Volume 10, Issue 6, June – 2025 International Journal of Innovative Science and Research Technology
ISSN No:-2456-2165 https://doi.org/10.38124/ijisrt/25jun567

Assessment of Flow Dynamics of a 5-Digit Series Airfoil with Variable Aerodynamic Parameters

Nwanwa Vivian C.[1]; Okon Aniekan A.[2]; Asuquo, Idongesit O.[3]

[1]Department of Mechanical and Aerospace Engineering, University of Uyo, Nigeria
[2]Department of Mechanical and Aerospace Engineering, University of Uyo, Nigeria
[3]Department of Mechanical and Aerospace Engineering, University of Uyo, Nigeria

Publication Date: 2025/06/20

Abstract: An airfoil is the cross-sectional shape of a wing, blade, or sail, designed to generate aerodynamic forces as it moves through the air. When interacting with airflow, an airfoil generates lift and drag forces. To standardize airfoil design, the National Advisory Committee for Aeronautics (NACA) developed various airfoil families, with extensive studies focused primarily on the 4-digit series. However, limited attention has been given to the aerodynamic behaviour of the 5-digit series. This study assesses the aerodynamic performance of the NACA 23012, a 5-digit airfoil, under varying Reynolds numbers and angles of attack to establish its suitability for high performance wind turbind. Computational Fluid Dynamics (CFD) simulations were conducted at angles of attack (AoA) of 8°, 12°, 16°, 20°, and 24°, with Reynolds numbers of 3.0×10^6, 6.0×10^6, and 8.8×10^6. The objective was to identify the conditions that yield optimal performance in terms of lift-to-drag ratio (L/D), coefficient of lift (CL), and coefficient of drag (CD). Results showed an increase in lift with increasing AoA up to a critical range between 12° and 16°, beyond which flow separation and stall effects reduced aerodynamic efficiency. The optimal performance was observed at an 8° angle of attack and Reynolds number of 8.8×10^6, where a high lift coefficient and relatively low drag resulted in a favourable lift-to-drag ratio. A linear regression analysis revealed an insignificant variation between CFD results and standard experimental values, validating the simulation accuracy. These findings provide valuable insights for blade design aimed at enhancing aerodynamic efficiency in wind turbines, ultimately improving torque generation, power output, and overall system performance.

Keywords: *NACA 23012 Airfoil; Angle of Attack; Reynolds Number; Lift-to-Drag Ratio; Computational Fluid Dynamics (CFD).*

How to Cite: Nwanwa Vivian C.; Okon Aniekan A.; Asuquo, Idongesit O. (2025) Assessment of Flow Dynamics of a 5-Digit Series Airfoil with Variable Aerodynamic Parameters. *International Journal of Innovative Science and Research Technology*, 10(6), 1157-1179. https://doi.org/10.38124/ijisrt/25jun567

I. INTRODUCTION

Energy is vital for economic and social growth and development in today's world. It is therefore necessary to have access to reliable and affordable energy. However, energy production and consumption contribute substantially to the release of greenhouse gases and global warming, with disastrous environmental effects, [1], [2]. Balancing the increasing energy demand with a reliable and sustainable supply is a challenging task. Expanding energy sources, while enhancing energy efficiency during production and consumption remain key strategies to strengthen energy security to meet the growing demand [3]. Many countries of the world including Nigeria are blessed with plentiful renewable energy resources like wind, solar, marine energy etc. These sources form the bedrock of the nation's sustainable energy plans, [4], as the world matches towards the zero-carbon future. Wind energy is among the leading renewable sources and wind turbines (Figure 1), play a critical role in converting the natural motion of the wind to mechanical energy thereby generating electricity, [5], [6]. Based on aerodynamic forces, wind turbines are classified into lift-based and drag-based turbines. Lift-based turbines, such as the horizontal axis wind turbine (HAWT) and the Darrieus vertical axis wind turbine (VAWT), are more efficient compared to drag-based turbines like the Savonius wind turbine, which is valued for its simplicity [7]. Most vertical axis wind turbines are drag-based, however, the Darrieus wind turbine (Figure 2), despite being a vertical axis turbine, operates on a lift-based principle and offers superior performance compared to other vertical axis turbines [8]. The performance of these turbines is largely dependent on the geometry of the turbine blades. An airfoil is the cross-sectional shape of a wing, blade, or sail, designed to generate aerodynamic forces as it moves through the air [9]. When a body of this type interacts with the airflow, it experiences two main aerodynamic forces, lift, directed orthogonal to the flow and drag, directed parallel to it, [10].

ISSN No:-2456-2165 https://doi.org/10.38124/ijisrt/25jun567

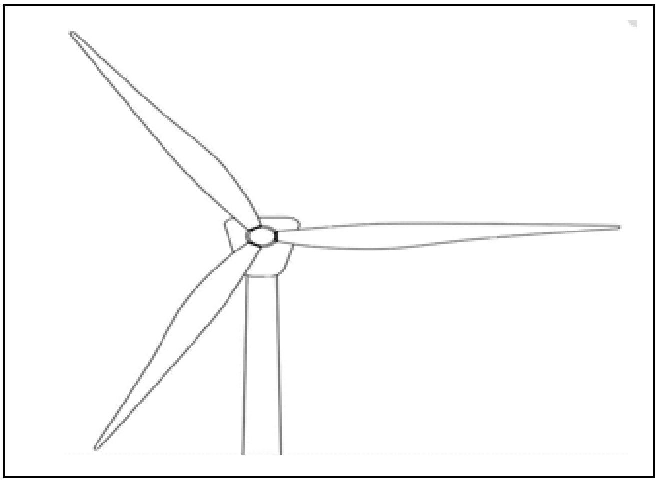

Fig 1 A 3-Bladed Wind Turbine

The size and action of these forces are mainly controlled by the physical profile of the airfoil geometry, including camber, thickness distribution, and leading-edge radius. To facilitate systematic airfoil design and analysis, the National Advisory Committee for Aeronautics (NACA) developed standard airfoil families, categorized using numerical series. The widely known NACA 4-digit and 5-digit series describe airfoil profiles using mathematical formulas, where each digit encodes specific shape parameters [11]. For instance, NACA 23012 belongs to the 5-digit series and is frequently used in both aviation and wind energy applications. Its cross-sectional profile and aerodynamic properties can be generated using the defined NACA equations [12]. The NACA airfoils have been fundamental in the advancement of both aviation and renewable energy technologies. The design of airfoils has always brought to light systematic (mathematical) formulations through which shape parameters can be controlled, contributing to the prediction and optimization of aerodynamic performance over a wide range of operating conditions [11]. The aerodynamic behaviour of an airfoil is described by three key parameters which are the coefficient of lift (Cl), the coefficient of drag (Cd), and the lift-to-drag ratio (Cl/Cd) [13]. These parameters differs with the angle of attack (AoA) and the Reynolds number, which is a function of airspeed, air density, and the chord length of the airfoil. An airfoil that produces high lift with minimal drag is ideal for efficient energy conversion, whether in aircraft wings or wind turbine blades [10].

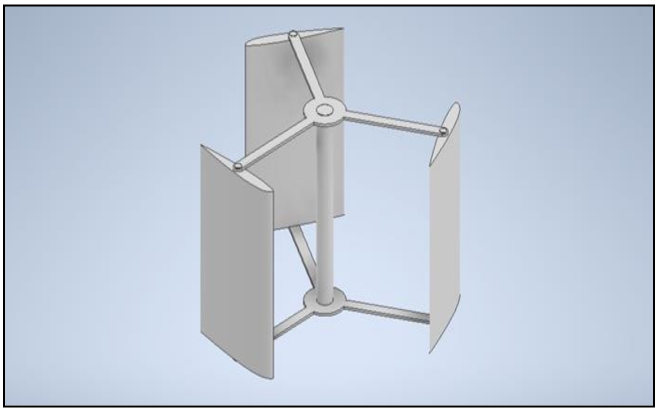

Fig 2 A 3-Bladed Darrieus Wind Turbine

Several researchers have utilized Computational Fluid Dynamics (CFD) techniques to investigate the aerodynamic behaviour of various NACA airfoils under different flow conditions. These studies provide valuable insights into the lift and drag characteristics, stall behaviour, and suitability of specific airfoils for different engineering applications. Simulation on NACA 0012 using ANSYS Fluent at Reynolds numbers ranging from 1×10^5 to 1×10^6 and angles of attack from -10° to +20° showed that maximum lift occurred at around 12° AoA [14]. NACA 4412 simulation showed that the k-ω SST turbulence model gave the most accurate results in predicting stall also, the maximum Cl/Cd was observed between 8°–10° AoA [15]. Analysis of the lift and drag forces on a NACA 0012 airfoil showed a correlation between increasing Reynolds numbers and enhanced lift and drag forces [16]. The study validated computational results against experimental data from Sandia National Laboratories, reinforcing computational analysis reliability in aerodynamic performance analysis. [17] Further explored the effects of increasing the angle of attack on a NACA 0012 airfoil, observing a rise in lift coefficient until flow separation occurs beyond a critical angle. The simulation and wind tunnel tests carried out on NACA 0015 airfoil [18], demonstrated that helical blade designs reduce torque ripple and improve startup. [19], compared the performances of NACA 0012, NACA 0021, and NACA 0018 at different tip speed ratios. The result showed that thicker airfoils perform better at low Reynolds numbers due to delayed stalls. Similarly, [20], evaluated H-type VAWTs with NACA 0012, S1046, and NACA 0024 airfoils. The simulation showed that airfoil choice significantly impacts power coefficient and stall characteristics. From the contributions to the knowledge frontiers so far examined, many studies have been carried out in 4-series NACA airfoils as compared to their 5-series counterparts. The continuous search for enhanced efficiency in renewable energy conversion has necessitated the assessment of the performance of higher series of NACA airfoils to unlock the hidden knowledge in them that are yet to be unraveled. This study therefore assesses the aerodynamic performance of a 5-series NACA 23012 airfoil with variable Reynolds numbers and angles of attack, to provide more insight into wider applicability for smart turbine blades. The NACA 23012 airfoil, a member of the 5-digit series, was selected over commonly used 4-digit profiles for this research because the 5-digit series was specifically designed for higher lift coefficients at lower angles of attack compared to 4-digit airfoils, which is important for self-starting behaviour in small-scale wind turbines. NACA 23012 being a cambered airfoil provides positive lift at zero or near-zero AoA, improving start-up torque and cut-in wind speed performance of a turbine. Unlike symmetric airfoils (e.g., NACA 0012, 0015) that generate zero lift at 0° AoA. [17], [18].

II. MATERIALS AND METHODS

The airfoil model for this study was NACA 23012, with its coordinates obtained from the Airfoil Tool database, [20]. NACA 23012, a five-digit series airfoil, was originally designed for aircraft applications requiring low drag at

ISSN No:-2456-2165 https://doi.org/10.38124/ijisrt/25jun567

moderate lift coefficients [11] but has since been adapted for wind turbine blades due to its favourable aerodynamic characteristics. The number '23012' represents a specific camber and thickness configuration, a moderate forward camber and a 12% thickness-to-chord ratio, which enables it to produce substantial lift while maintaining acceptable drag levels [12]. Table 1 shows the details of the airfoil used for the study. The Shear Stress Transport (SST) k-ω turbulence model was chosen for this study over other common models like k- Ɛ (k epsilon) due to the fact that SST k-ω provides enhanced resolution of boundary layer separation and adverse pressure gradients, which are necessary for correctly predicting stall and lift behaviour on airfoils at high angles of attack. Studies show that SST k-ω outperforms Spalart-Allmaras and standard k-Ɛ in capturing stall onset and post-stall behaviour [27], which is also a consideration in this study.

Table 1 Airfoil Parameters

Airfoil Details	**NACA 23012**
Maximum thickness	12%
Maximum Camber Position	15%
Camber type	Normal (not reflexed)
Design CL	0.2
Trailing edge	Standard NACA sharp
Symmetry	Non
Data source	UIUC Airfoil Database

➢ *Computational Setup and Mesh*

The CFD simulation was performed using ANSYS Fluent. This CFD package was chosen because of its high accuracy and flexibility. The airfoil was simulated at varying angles of attack: 0°, 8°, 12°, 16°, 20°, and 24° and three Reynolds numbers: 3.0*10^6, 6.0*10^6 and 8.8*10^6. The higher Reynolds number range was chosen since the NACA 23012 airfoil is well-suited for high-power turbines, [21]. A C-type fluid domain was used, since it is common in most aerodynamics simulations, its better handling of boundary layers, improved resolution near walls and reduced numerical dissipation in flow directions, [22], [23]. The geometry was setup, and meshing was carried out with appropriate refinement to ensure an accurate analysis of fluid dynamics along the turbine. The computational analysis and the results duration depended on the mesh characteristics. From the mesh statistics shown in Figure 4, the number of nodes was 155720 with 155000 elements. The geometry of the airfoil is shown in Figure 3.

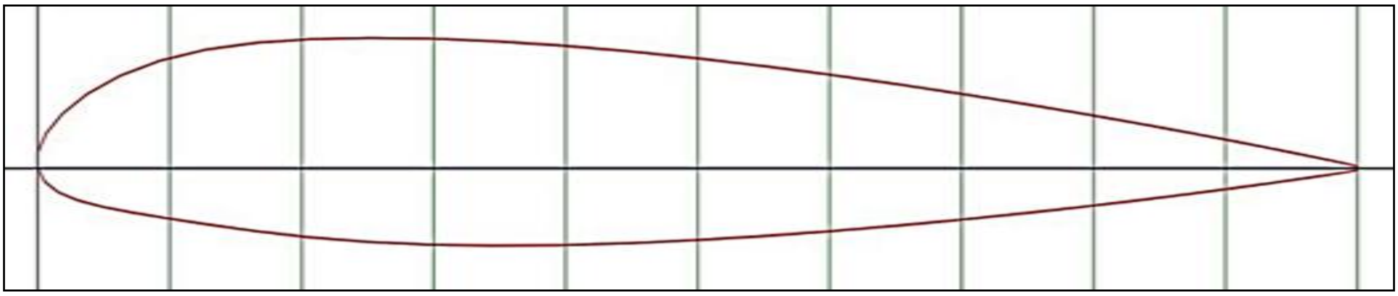

Fig 3 NACA 23012 Airfoil

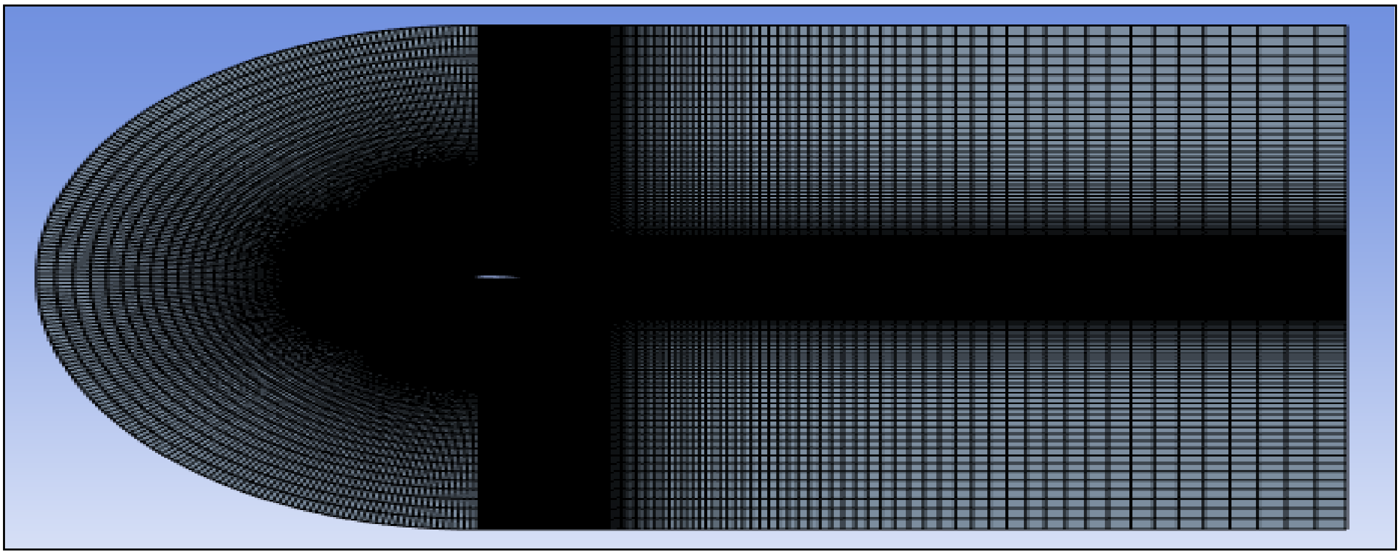

Fig 4 Mesh Refinement around the Airfoil

ISSN No:-2456-2165 https://doi.org/10.38124/ijisrt/25jun567

Boundary conditions for the 2D simulation of the airfoil is seen in Table 2. The boundary conditions define how the fluid interacts with the domain boundaries. They are crucial for obtaining accurate and realistic simulation results.

Table 2 Boundary Conditions

Input Parameters	Magnitude
Solver type	Pressure based
Time	Steady
Viscous model	SST k-omega
Fluid	Air
Density (kg/m3)	1.225
Viscosity (kg/m-s)	1.7894e-05
Turbulent viscosity	1
Angle of Attack	0, 8, 12, 16, 20, 24.
Reynold number	3.0*10^6, 6.0*10^6, 8.8*10^6
Number of iterations	1000
Chord-length	0.36m
Momentum	Second Order Upwind
Pressure velocity coupling	Simple

III. RESULTS AND DISCUSSIONS

The results obtained from the simulations of the airfoil is discussed in this section. The simulations were done at varying angle of attacks and Reynolds number. The findings are structured to provide a detailed analysis on the aerodynamics performance of the airfoil under flow conditions.

A. Static Pressure Variability with Parameters

Contour plots are used to visualize pressure and velocity in fluid flow because they provide a clear and self-explanatory way to observe how these variables change across a surface or domain. They help to identify key flow features like high and low pressure zones, flow separation, and wake formation [24]. In this case, contour was used to show effective comparison between different angles of attack and Reynolds numbers.

➢ *Pressure Contour for Re = 3.0×10^6*

Figure 5 shows pressure contour plots around a NACA 23012 airfoil at Reynolds number 3.0×10^6 and angle 0º, 8º, 12º, 16º, 20º, 24º. These contours illustrate how pressure distribution changes with increasing angle of attack, which in turn affects the aerodynamic performance of the airfoil. From observation, at 0º AoA, there is no significant pressure change between the upper and lower region as indicated by the blue/green colour contour. A distinct pressure gradient begins to form at angle 8º. The upper surface exhibits lower pressure (high suction), while the lower surface retains relatively higher pressure. This progresses through angle 12º as the low-pressure region on the upper surface becomes more pronounced. The pressure on the lower surface also increases, leading to a stronger pressure differential. This suggests that the airfoil is producing high lift, and the flow remains largely attached.

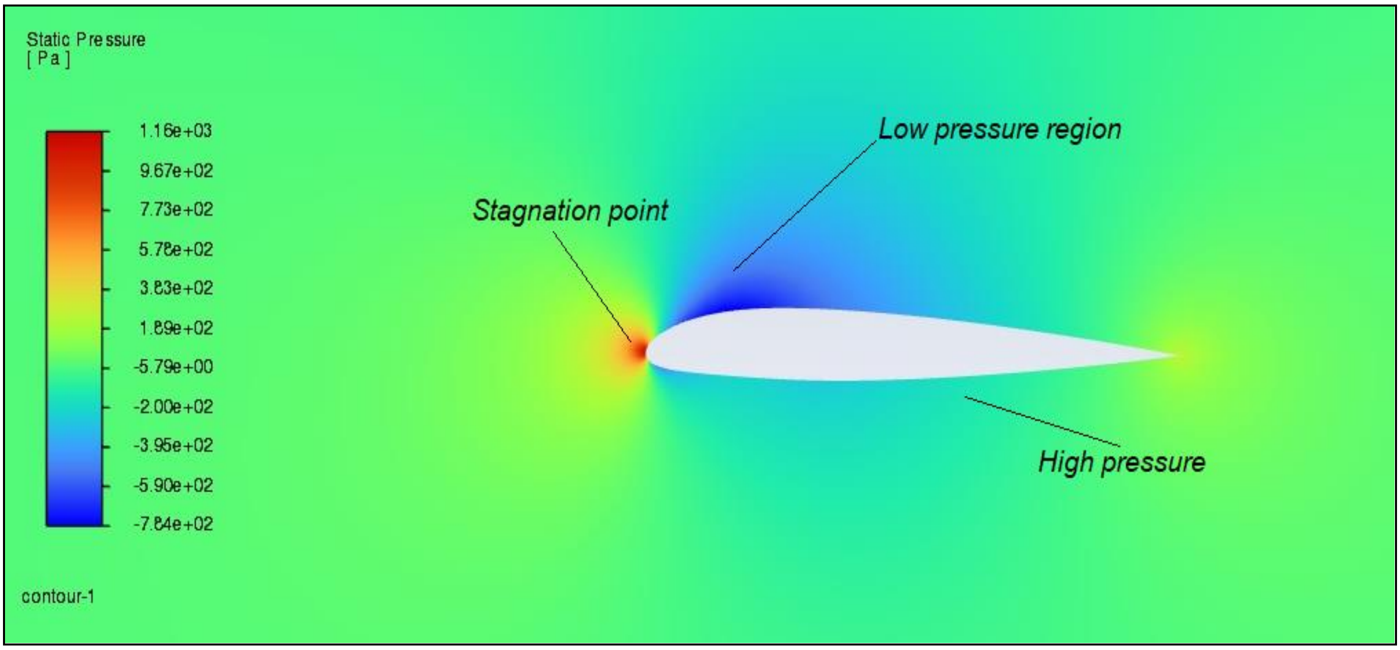

(a) 0º angle of attack at Re = 3.0×10^6

ISSN No:-2456-2165 https://doi.org/10.38124/ijisrt/25jun567

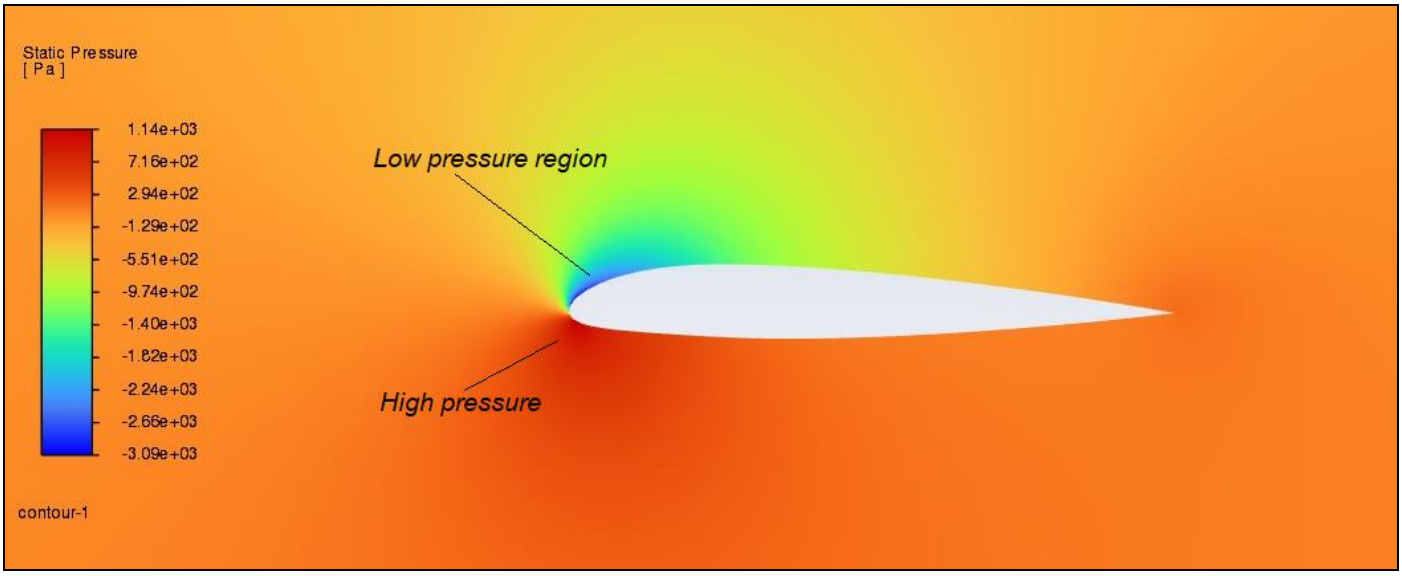

(b) 8° angle of attack at Re = 3.0×10^6

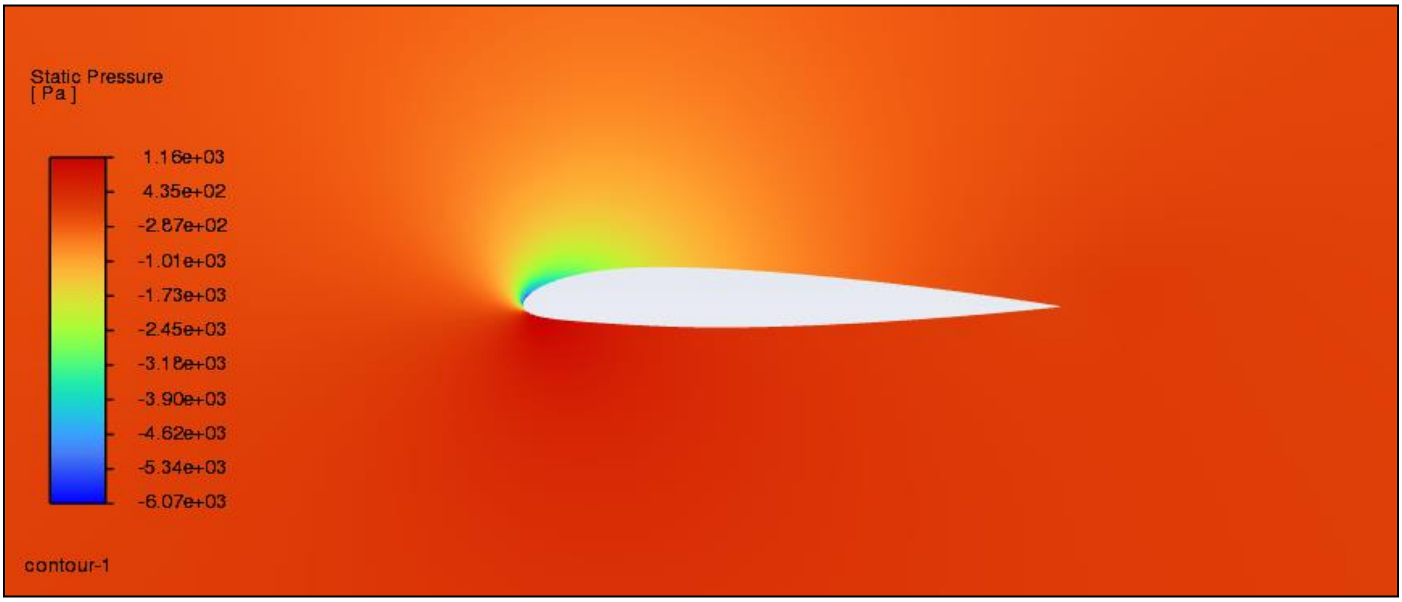

(c) 12° angle of attack at Re = 3.0×10^6

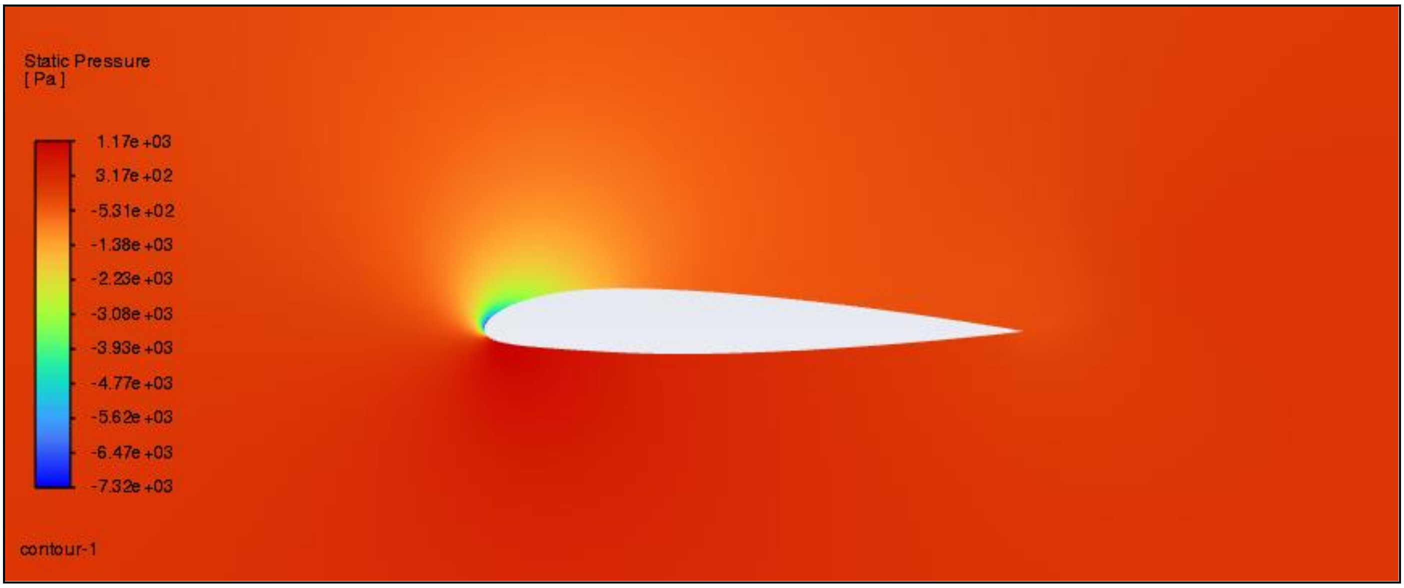

(d) 16° angle of attack at Re = 3.0×10^6

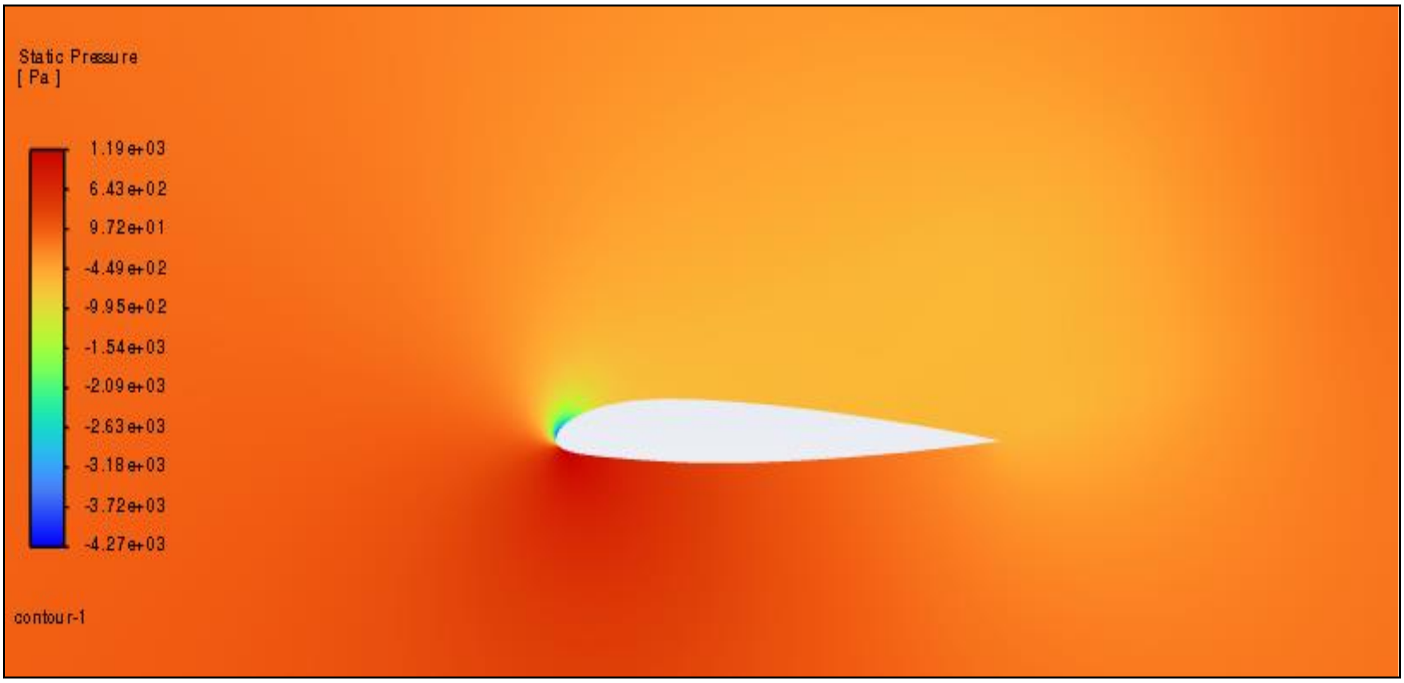

(e) 20^{0} angle of attack at Re = 3.0×10^{6}

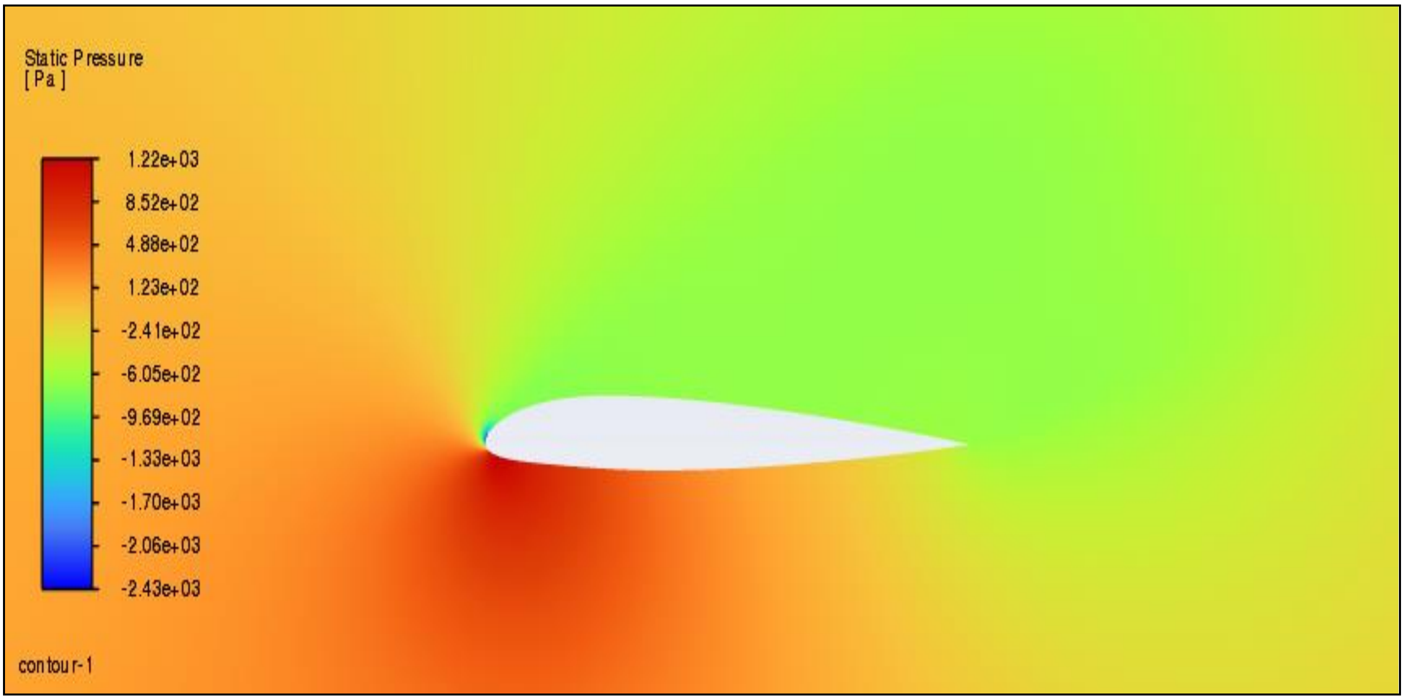

(f) 24^{0} angle of attack at Re = 3.0×10^{6}

Fig 5 Pressure Contour for Re = 3.0×10^{6}

At 16° AoA, the upper surface shows signs of pressure recovery that may suggest the onset of flow separation. The suction peak moves forward, and the pressure gradient becomes more adverse towards the trailing edge. This shows a near stall behavior. A significant region of uniform low pressure is visible on the upper surface at angle 20^{0} indicating large-scale flow separation. The flow separation becomes massive at angle 24^{0}. At this point, the pressure differential has diminished considerably, indicating a post-stall condition where the airfoil's lift has significantly dropped and drag has increased.

➢ *Pressure Contour for Re = 6.0×10^{6}*

Pressure distribution around NACA 23012 airfoil at different angles of attack and Reynolds number of 6.0×10^{6} is shown in Figure 6. At angle 0° angle of attack, the pressure distribution is relatively symmetrical above and below the airfoil. There is a high-pressure region near the leading edge on the lower surface, and a mild low-pressure region above the airfoil. This configuration generates minimal lift as there is little pressure difference.

International Journal of Innovative Science and Research Technology
ISSN No:-2456-2165
https://doi.org/10.38124/ijisrt/25jun567

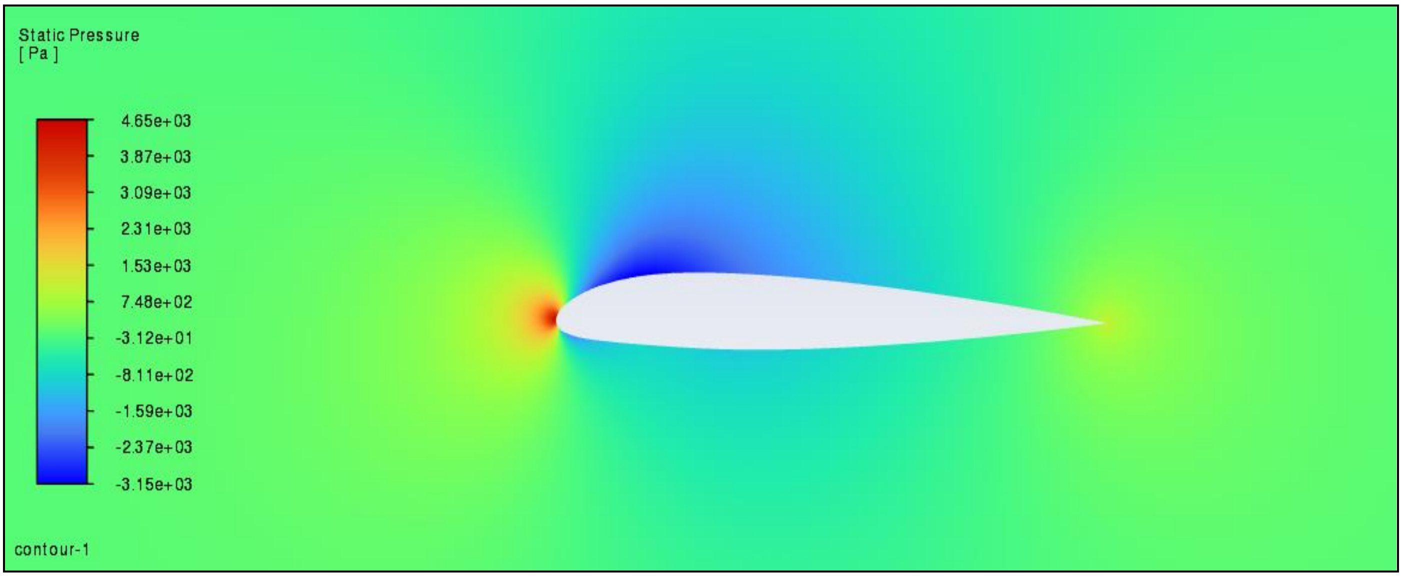

(a) 0º angle of attack at Re = 6.0×10⁶

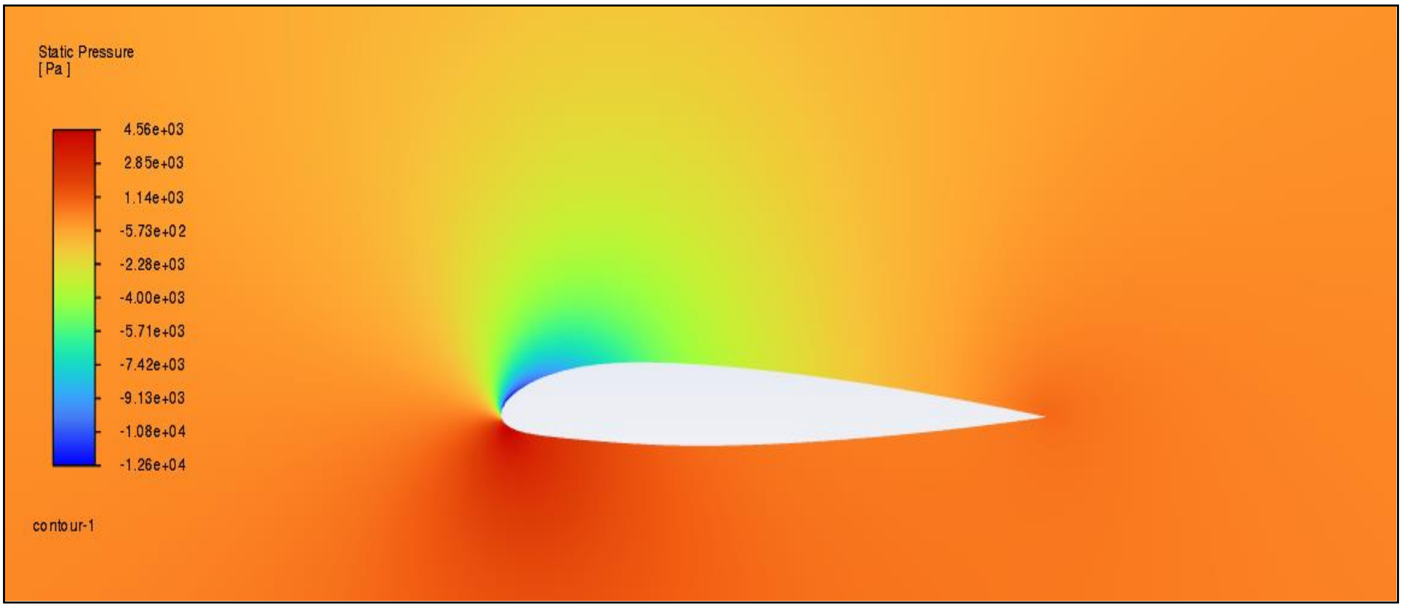

(b) 8º angle of attack at Re = 6.0×10⁶

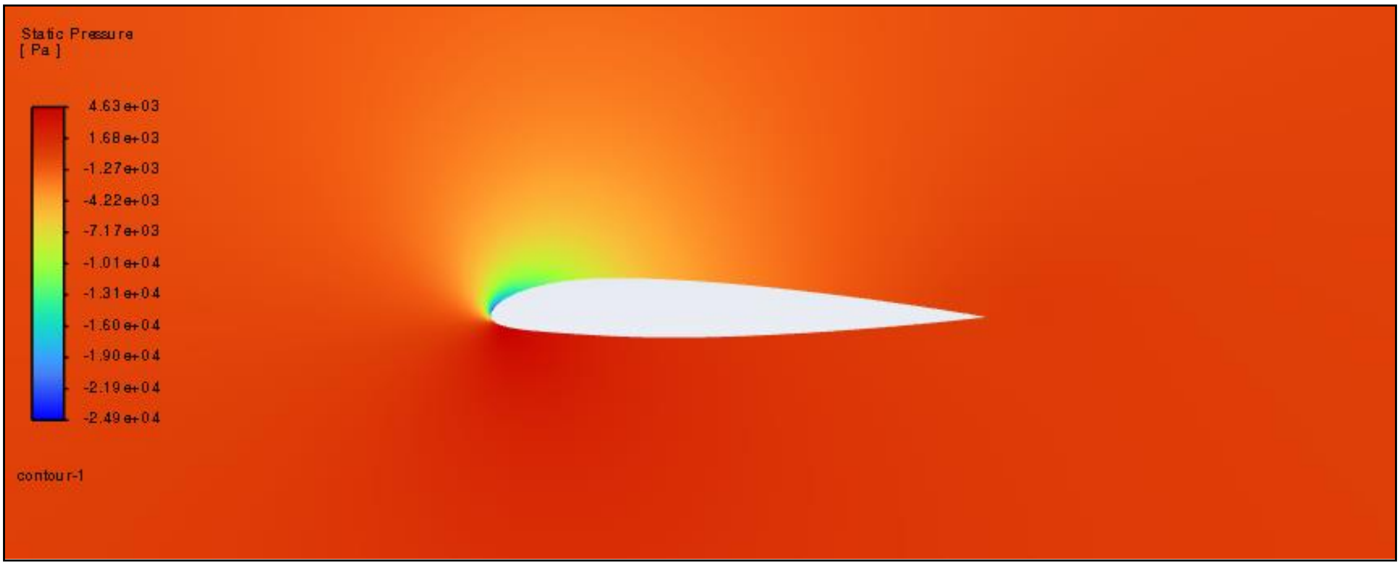

(c) 12º angle of attack at Re = 6.0×10⁶

ISSN No:-2456-2165 https://doi.org/10.38124/ijisrt/25jun567

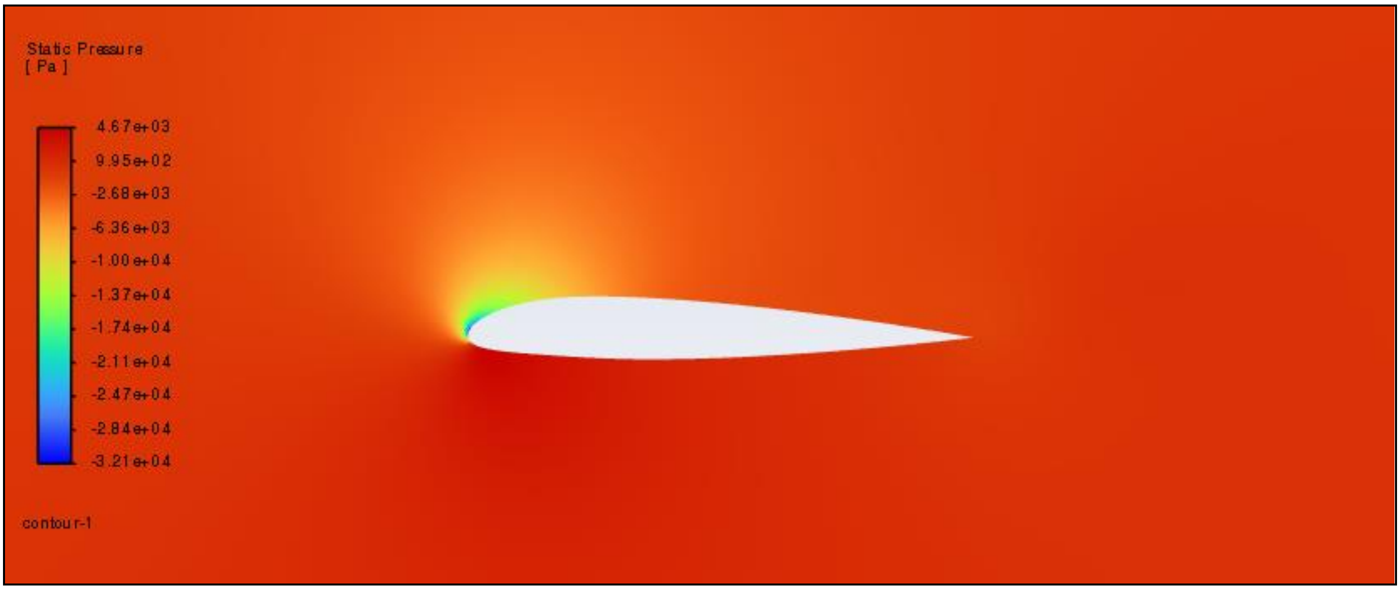

(d) 16⁰ angle of attack at Re = 6.0×10^6

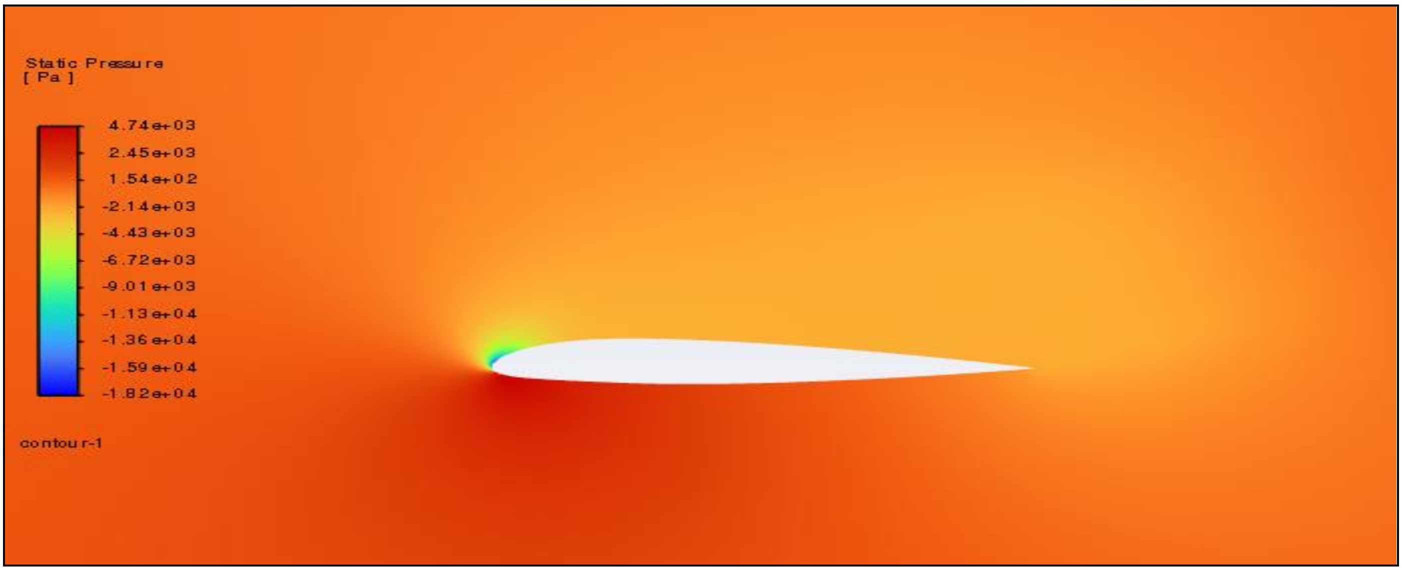

(e) 20⁰ angle of attack at Re = 6.0×10^6

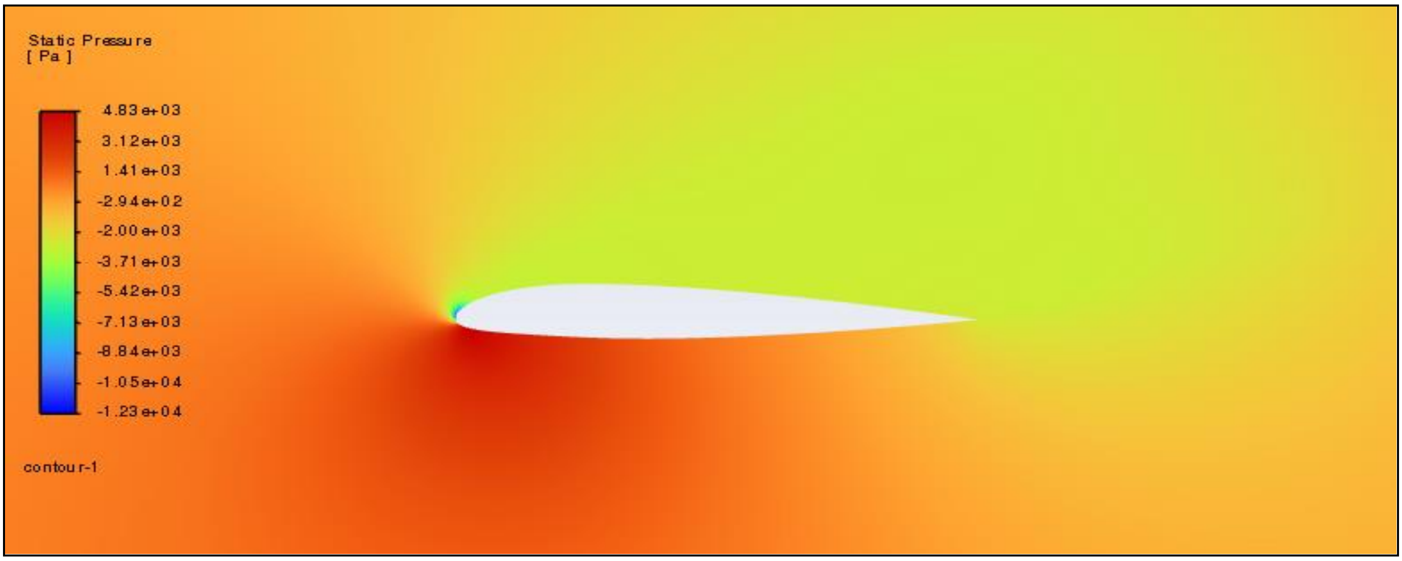

(f) 24⁰ angle of attack at Re = 6.0×10^6

Fig 6 Pressure Contour for Re = 6.0×10^6

ISSN No:-2456-2165 https://doi.org/10.38124/ijisrt/25jun567

When the angle increases to 8°, a pronounced low-pressure region develops on the upper surface of the airfoil, which intensifies the pressure difference between the upper and lower surfaces, resulting in an increased lift generation. At angle 12°, the low-pressure region on the upper surface becomes stronger and more concentrated near the leading edge. The pressure on the lower surface remains high, suggesting that the airfoil is operating at a high lift condition, possibly close to its maximum lift. As the angle of attack reaches 16°, the low-pressure region begins to weaken and spread toward the trailing edge. This indicates the onset of flow separation, where airflow starts detaching from the upper surface. At angle 20°, the pressure contours show a further weakening of the suction region, with a more uniform distribution over the upper surface. This suggests that the airfoil is experiencing stall. This progresses to angle 24º where the low-pressure region has almost disappeared, and the pressure distribution across the airfoil appears almost flat. This confirms a deep stall condition, where the flow is fully separated, resulting in minimal lift and very high drag.

- *Pressure Contour for Re = 8.8×10⁶*

Figure 7 shows the pressure contour at various AoA and Reynolds number 8.8×10^6. The pressure plot for angle 0º shows minimal pressure difference between the upper and lower surfaces, indicating that no effective lift is being generated. At angle 8º, a low-pressure region is observed on the upper surface near the leading edge, while the lower surface maintains higher pressure, indicating effective lift generation. The suction peak on the upper surface becomes more intense at angle 12º. The flow appears to still be attached, with no visible signs of flow reversal or large separation zones. At angle 16º, the pressure contours begin to flatten on the upper surface, suggesting the onset of flow separation. As it progresses to angle 20º, the upper surface displays signs of pressure recovery, which is typical of partial flow separation.

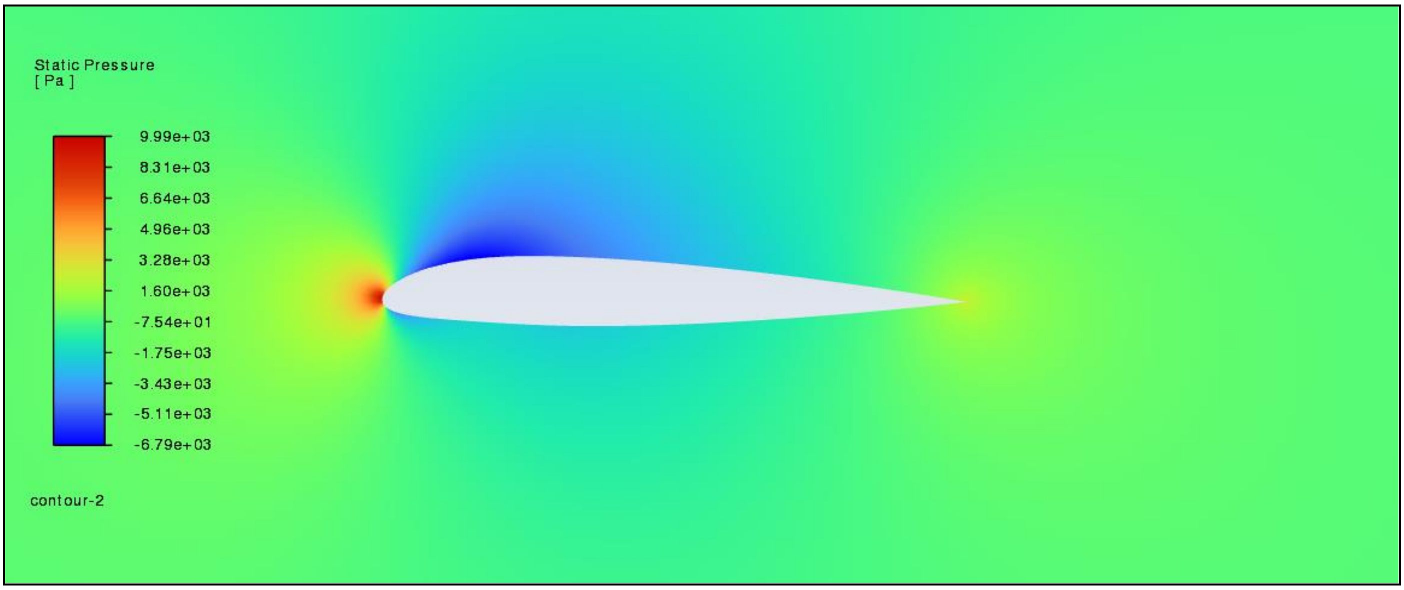

a) 0º angle of attack at Re = 8.8×10^6

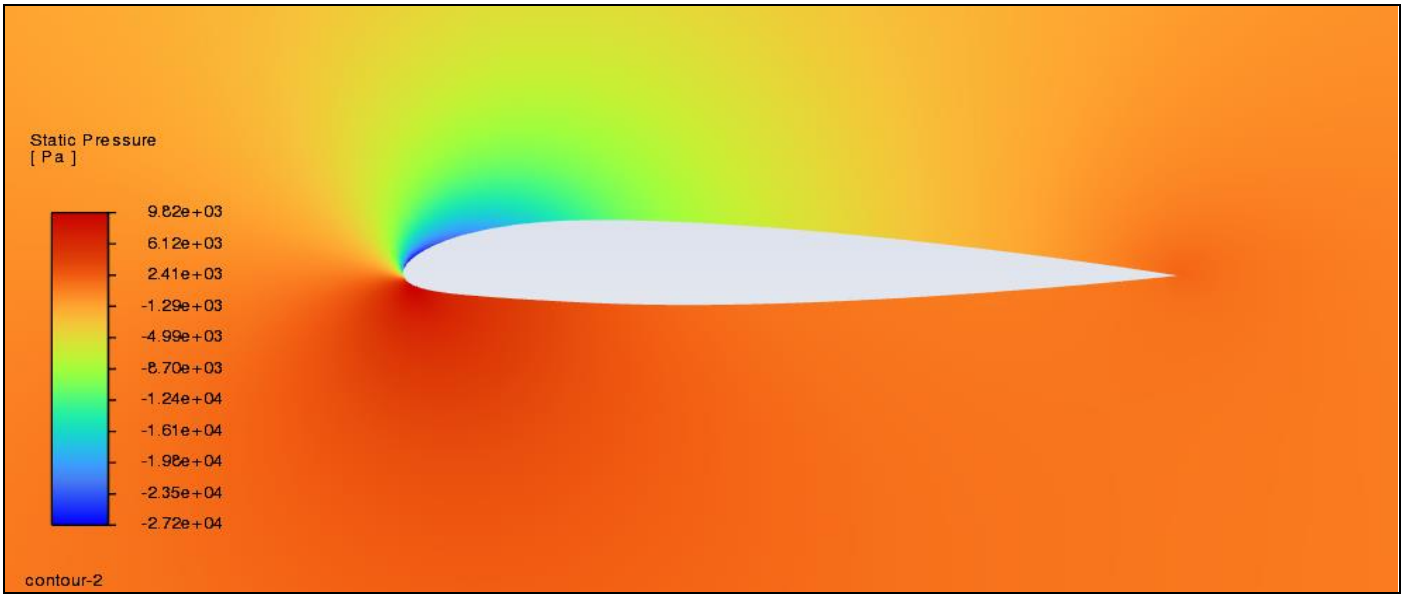

b) 8º angle of attack at Re = 8.8×10^6

ISSN No:-2456-2165 https://doi.org/10.38124/ijisrt/25jun567

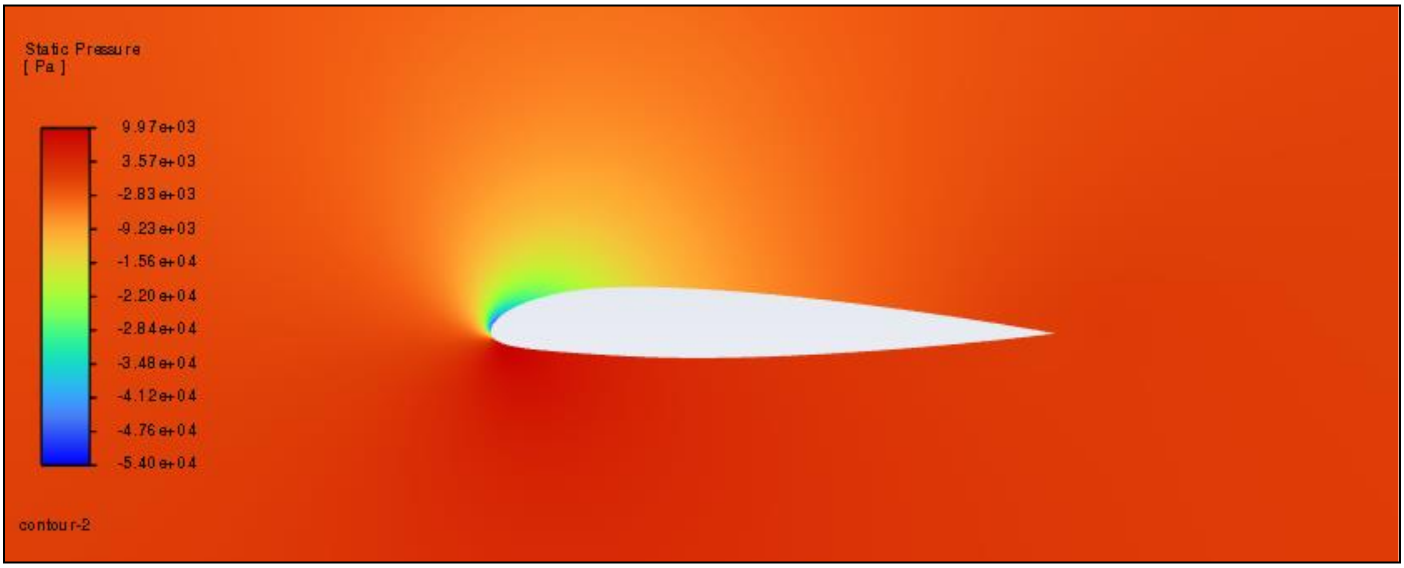

c) 12⁰ angle of attack at Re = 8.8×10^6

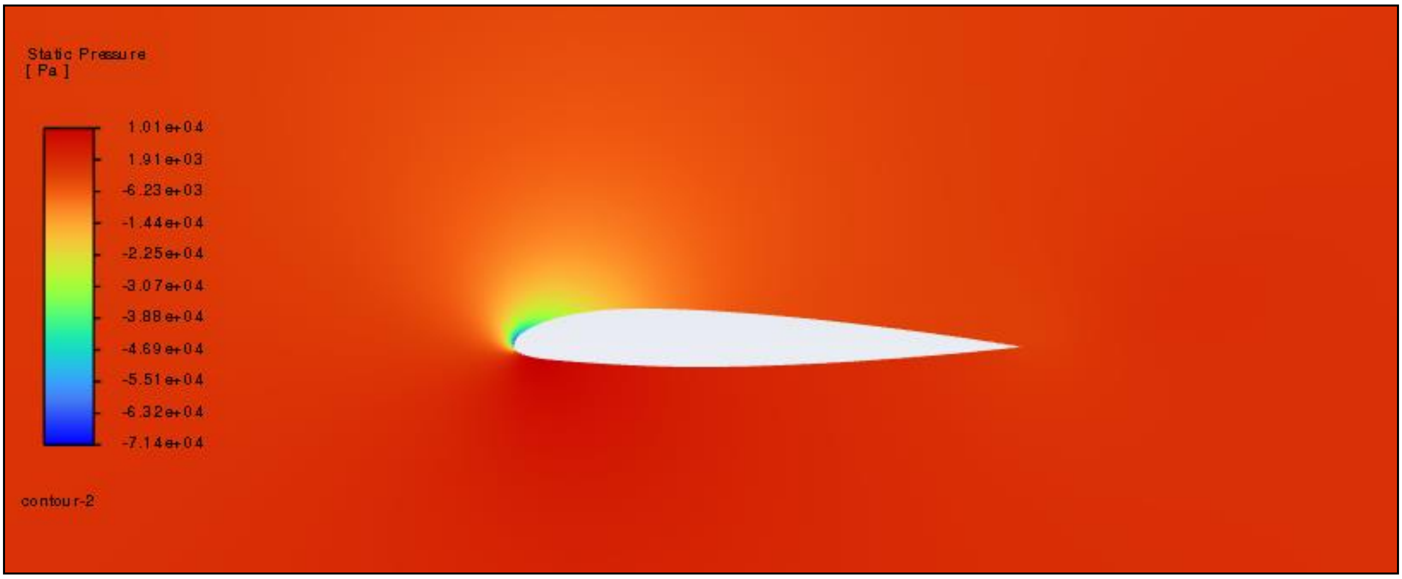

d) 16⁰ angle of attack at Re = 8.8×10^6

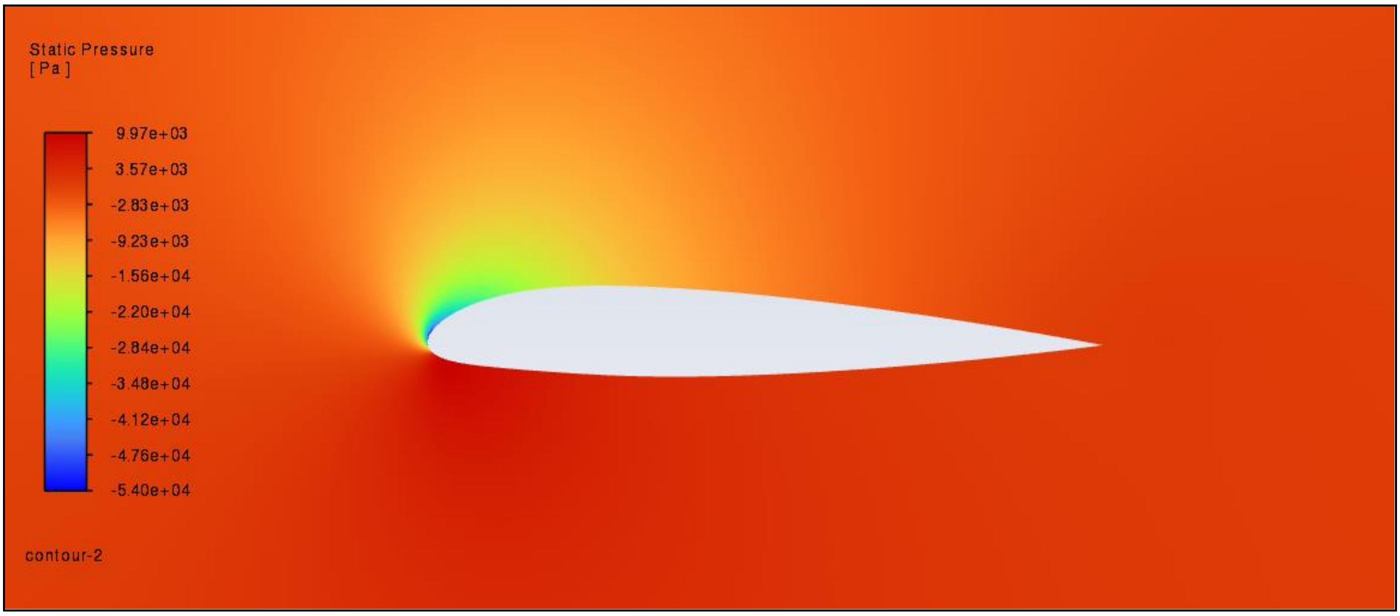

e) 20⁰ angle of attack at Re = 8.8×10^6

ISSN No:-2456-2165 https://doi.org/10.38124/ijisrt/25jun567

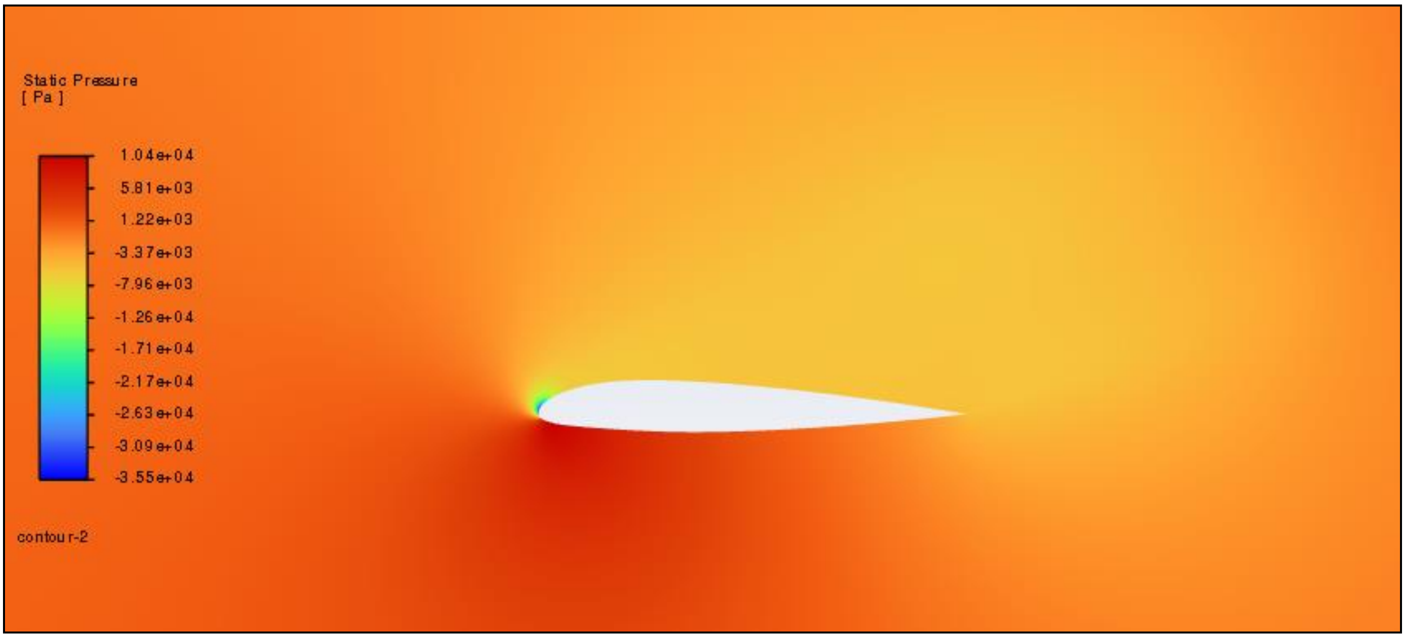

f) 24º angle of attack at Re = 8.8×10^6
Fig 7 Pressure Contour for Re = 8.8×10^6

At angle 24º, the pressure field on the upper surface shows a large, uniform low-pressure zone, indicating massive flow separation. The pressure difference between the upper and lower surfaces is reduced, confirming that the airfoil has stalled. This results in poor aerodynamic performance due to increased drag and loss of lift.

B. Velocity Variability with Parameters

This section presents velocity contours around a NACA 23012 airfoil at various angles of attack (AoA) at a Reynolds numbers. The contours are color-coded to represent airflow velocity magnitudes, with red and yellow indicating high velocity, and green to blue showing lower velocity or reversed flow.

- *Velocity Contour for Re = 3.0×10^6*

Figure 8 shows that, at 0° angle of attack, the flow is symmetric, and the velocity around the airfoil remains mostly uniform. The velocity increases significantly over the upper surface of the airfoil, shown by the intense yellow region, which suggests strong acceleration of airflow at AoA 8º. At 12°, the upper surface shows further signs of acceleration followed by flow deceleration, visible in the green and blue colors near the trailing edge. This transition suggests that a separation bubble is forming, and the boundary layer is detaching from the airfoil surface.

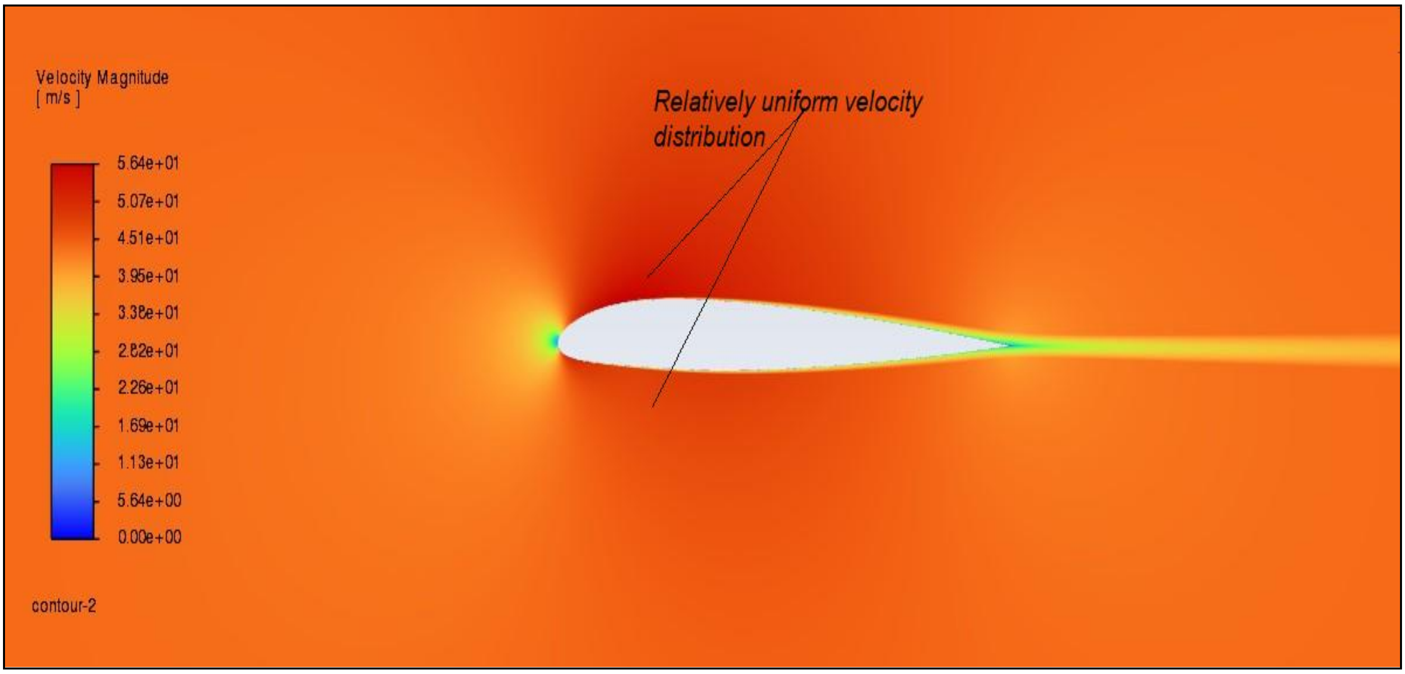

(a) 0º angle of attack Re = 3.0×10^6

ISSN No:-2456-2165 https://doi.org/10.38124/ijisrt/25jun567

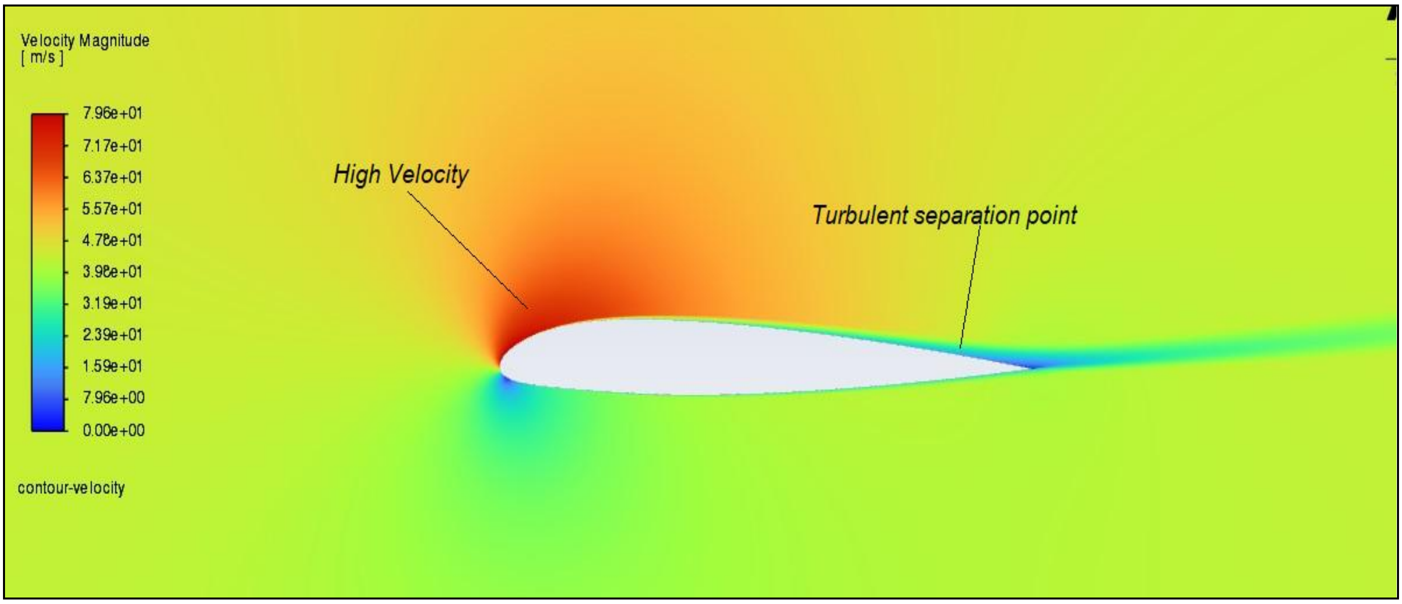

(b) 8º angle of attack Re = 3.0×10^6

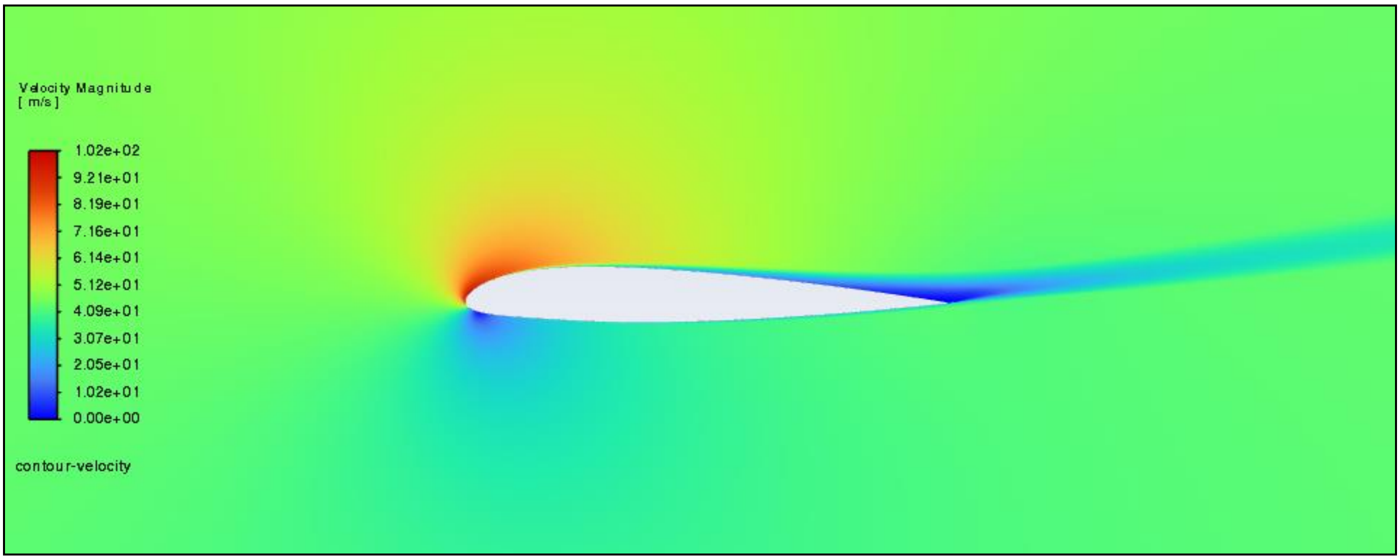

(c) 12º angle of attack Re = 3.0×10^6

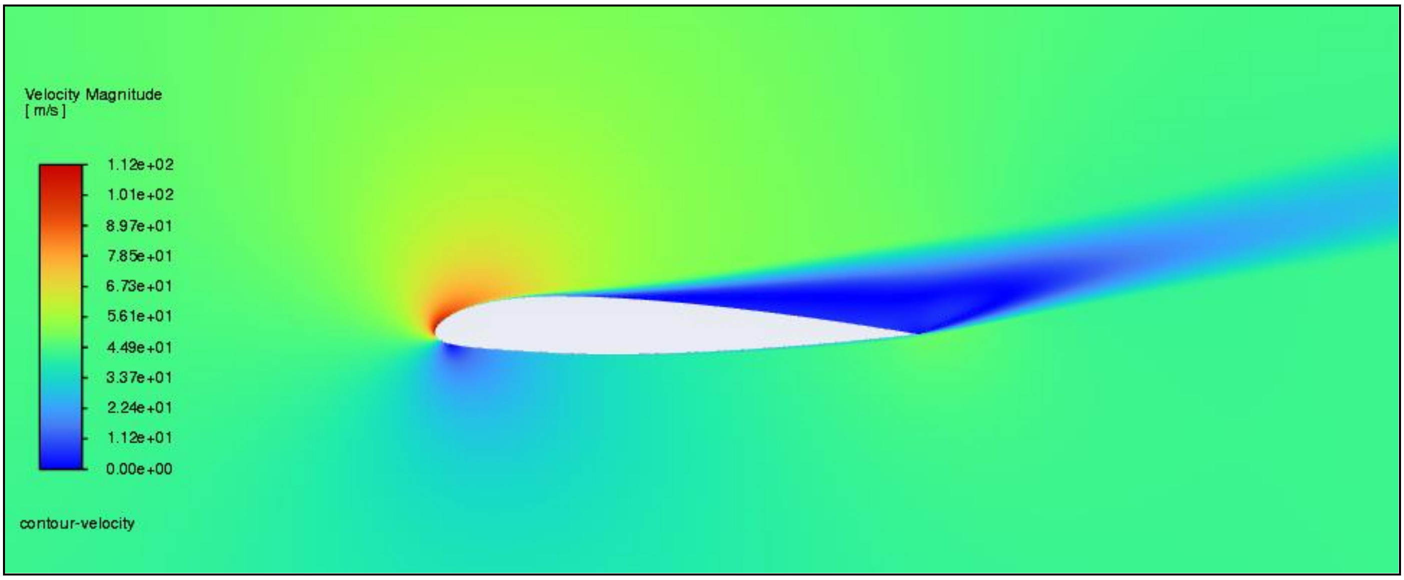

(d) 16º angle of attack Re = 3.0×10^6

ISSN No:-2456-2165 https://doi.org/10.38124/ijisrt/25jun567

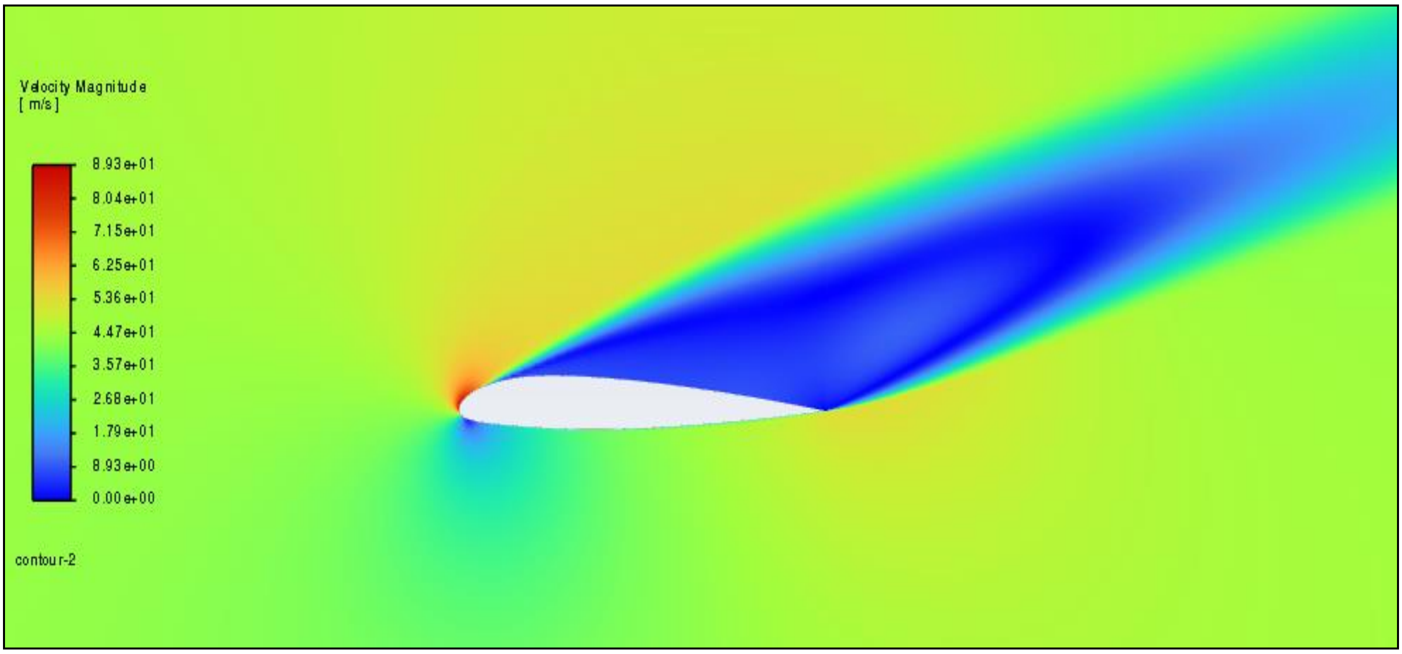

(e) 20⁰ angle of attack Re = 3.0×10^6

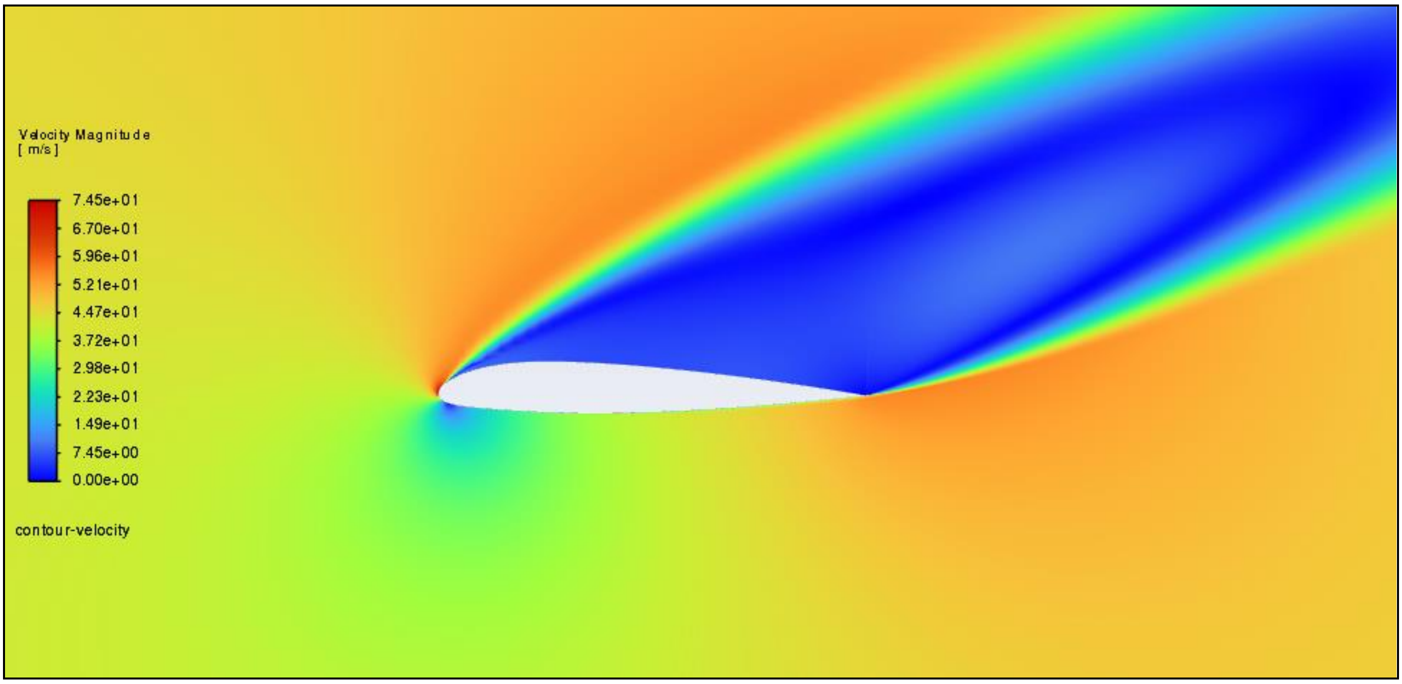

(f) 24⁰ angle of attack Re = 3.0×10^6

Fig 8 Velocity Contour for Re = 3.0×10^6

This flow separation continues through angle 16⁰ and grows even larger, extending from the mid-chord all the way to the trailing edge and into the wake at AoA 20⁰. At this angle, the flow is completely detached from the upper surface, suggesting stall. The stall becomes deeper at angle 24⁰ and the upper surface is dominated by low velocity.

➢ *Velocity Contour for Re = 6.0×10^6*

At 0° angle of attack, the flow around the airfoil is symmetric in Figure 9. The airflow accelerates smoothly over both the upper and lower surfaces, indicated by the orange and red shades. At angle 8°, the velocity over the upper surface increases significantly. The yellow region on the upper surface indicates the speedy airflow due to greater pressure difference. As it progresses through angle 12⁰, the upper surface continues to experience accelerated flow near the leading edge, but the velocity drops sharply toward the trailing edge. The blue and green colours in that region indicate that the flow is beginning to separate. At angle 16°, flow separation becomes more pronounced. The airfoil experiences stall at angle 20⁰, the flow over the upper surface is largely separated, shown by the wide blue region. There is no longer a smooth acceleration of airflow over the airfoil, and the wake is highly expanded and turbulent. The stall deepens at angle 24⁰.

ISSN No:-2456-2165 https://doi.org/10.38124/ijisrt/25jun567

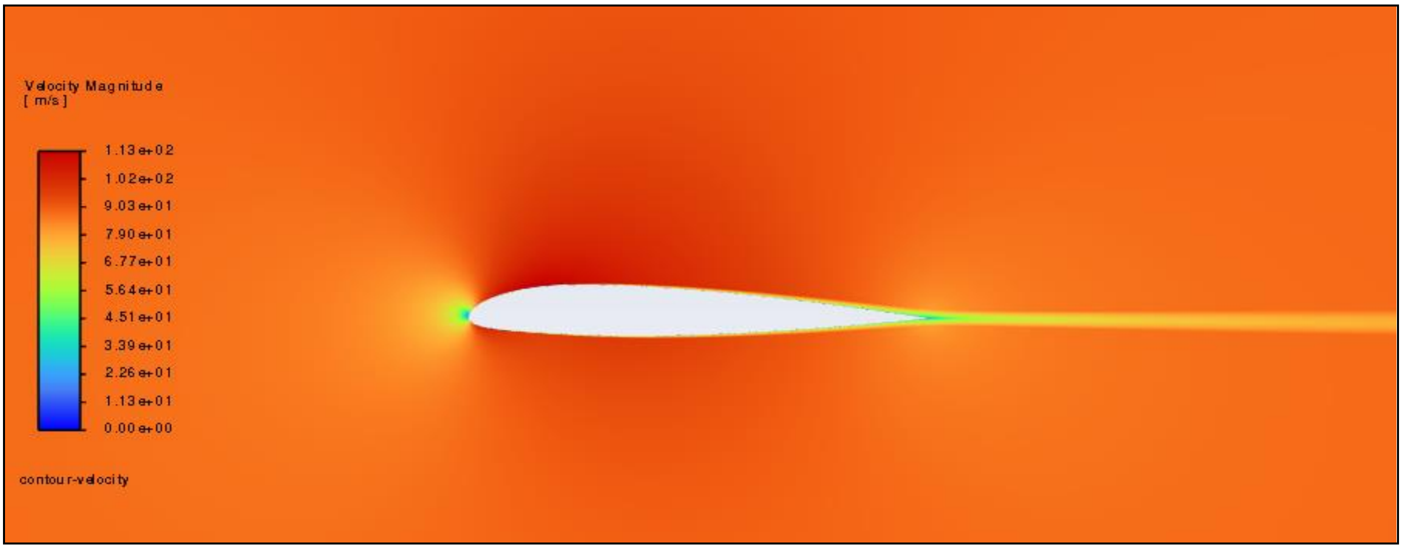

(a) 0º angle of attack Re = 6.0×10⁶

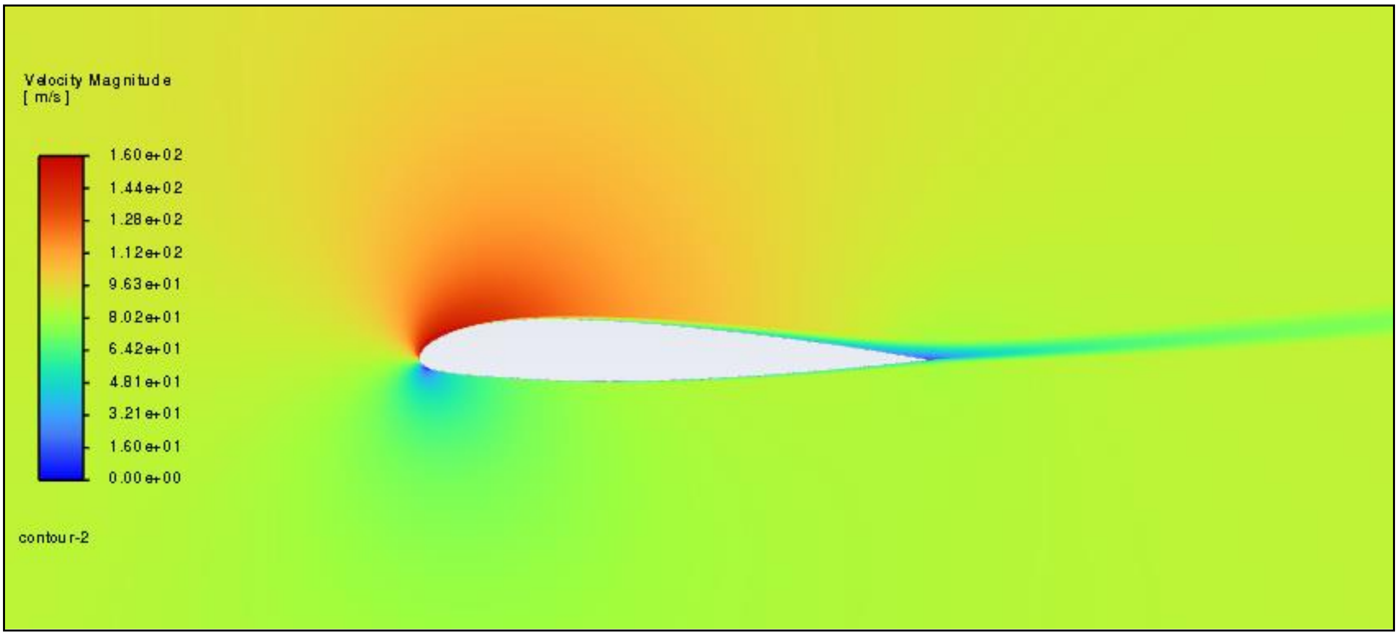

(b) 8º angle of attack Re = 6.0×10⁶

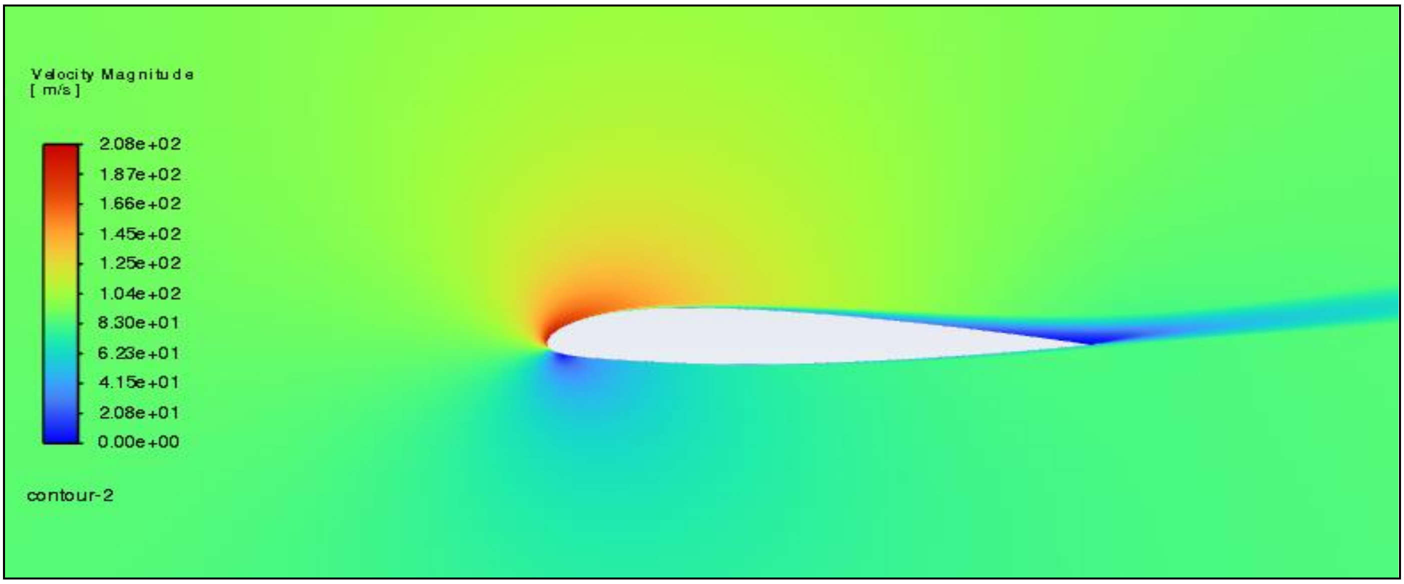

(c) 12º angle of attack Re = 6.0×10⁶

ISSN No:-2456-2165 https://doi.org/10.38124/ijisrt/25jun567

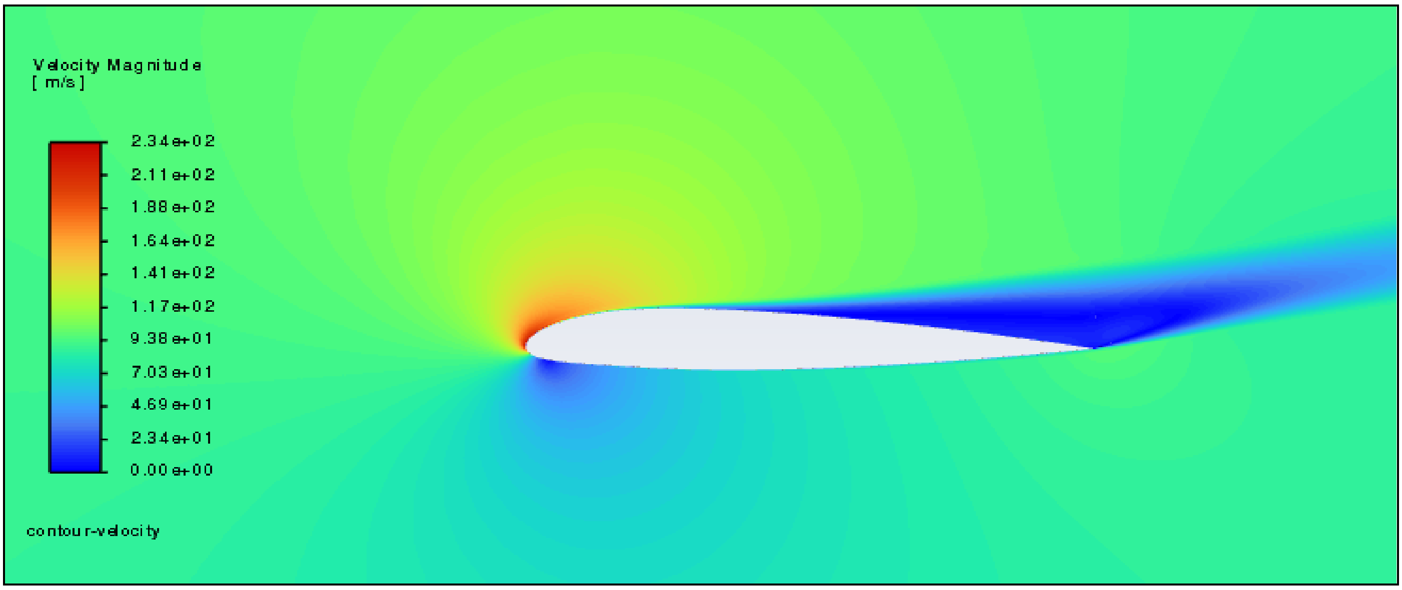

(d) 16° angle of attack Re = 6.0×10⁶

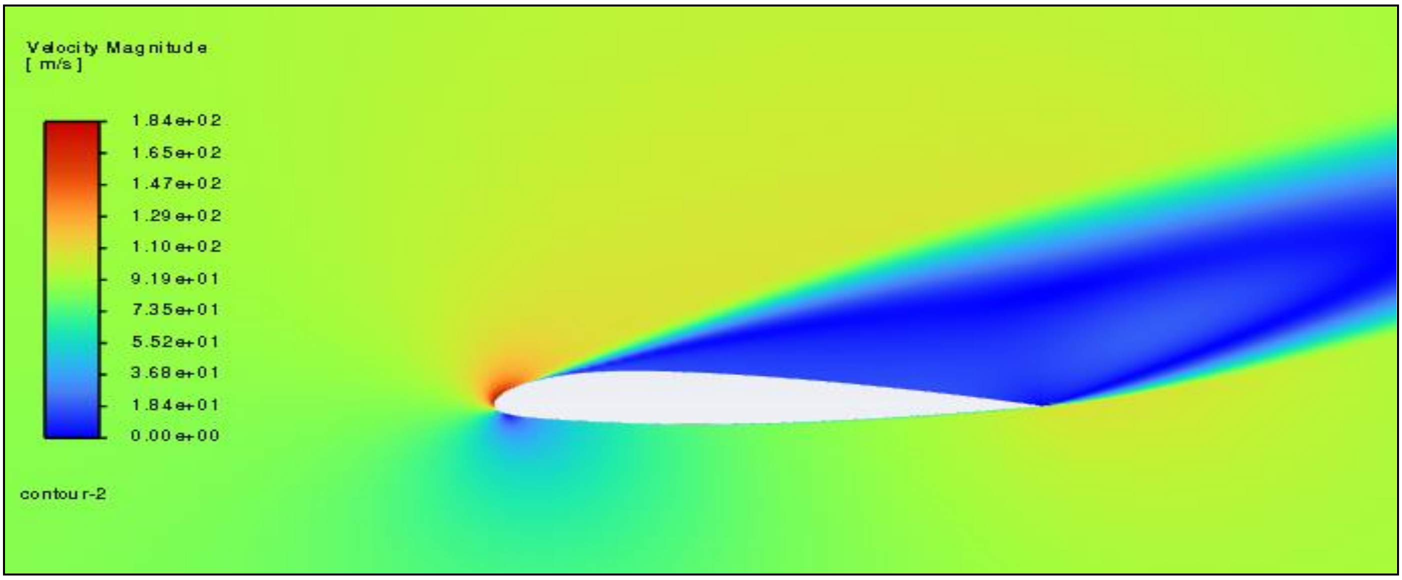

(e) 20° angle of attack Re = 6.0×10^6

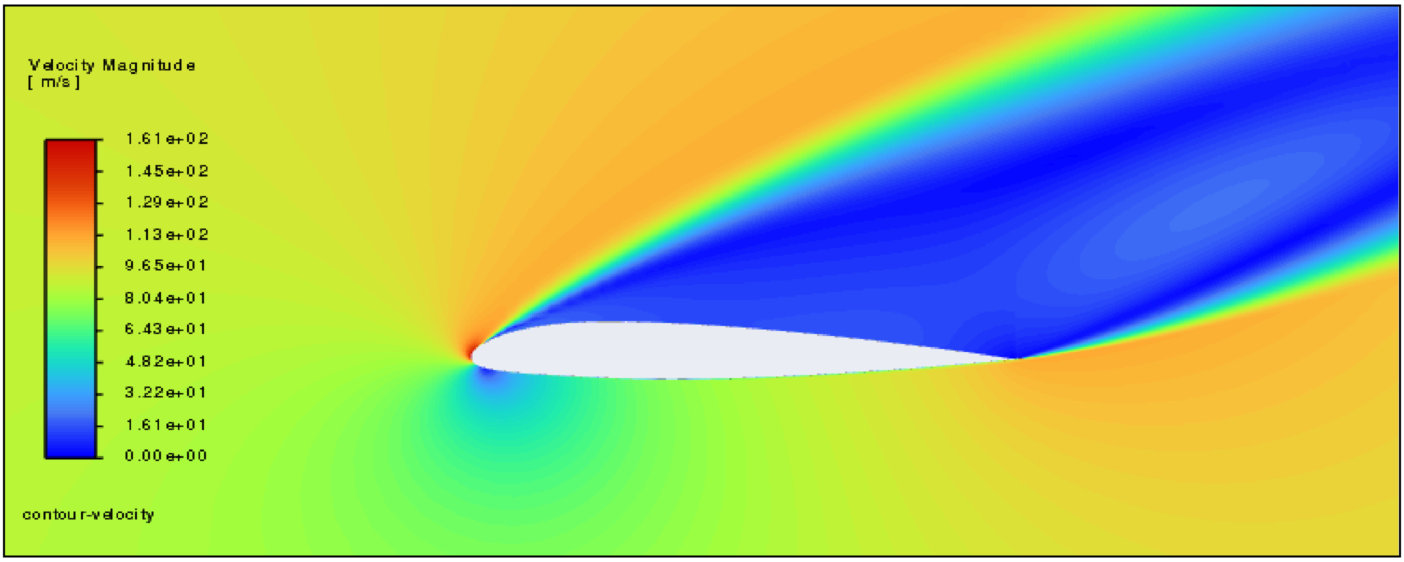

(f) 24° angle of attack Re = 6.0×10^6

Fig 9 Velocity Contour for Re = 6.0×10^6

ISSN No:-2456-2165 https://doi.org/10.38124/ijisrt/25jun567

➢ *Velocity Contour for Re = 8.8×10⁶*

In Figure 10, the velocity smoothly accelerates around the upper and lower surfaces until angle 8⁰ where the velocity in the upper surface increases significantly, with the contour showing shades of yellow indicating strong acceleration. At angle 12⁰, even as the front part remains in the yellow range, a blue zone begins to appear closer to the trailing edge, showing the onset of boundary layer separation. The blue region on the upper surface becomes more prominent at angle 16⁰ and expands backward into the wake, showing that separation has intensified.

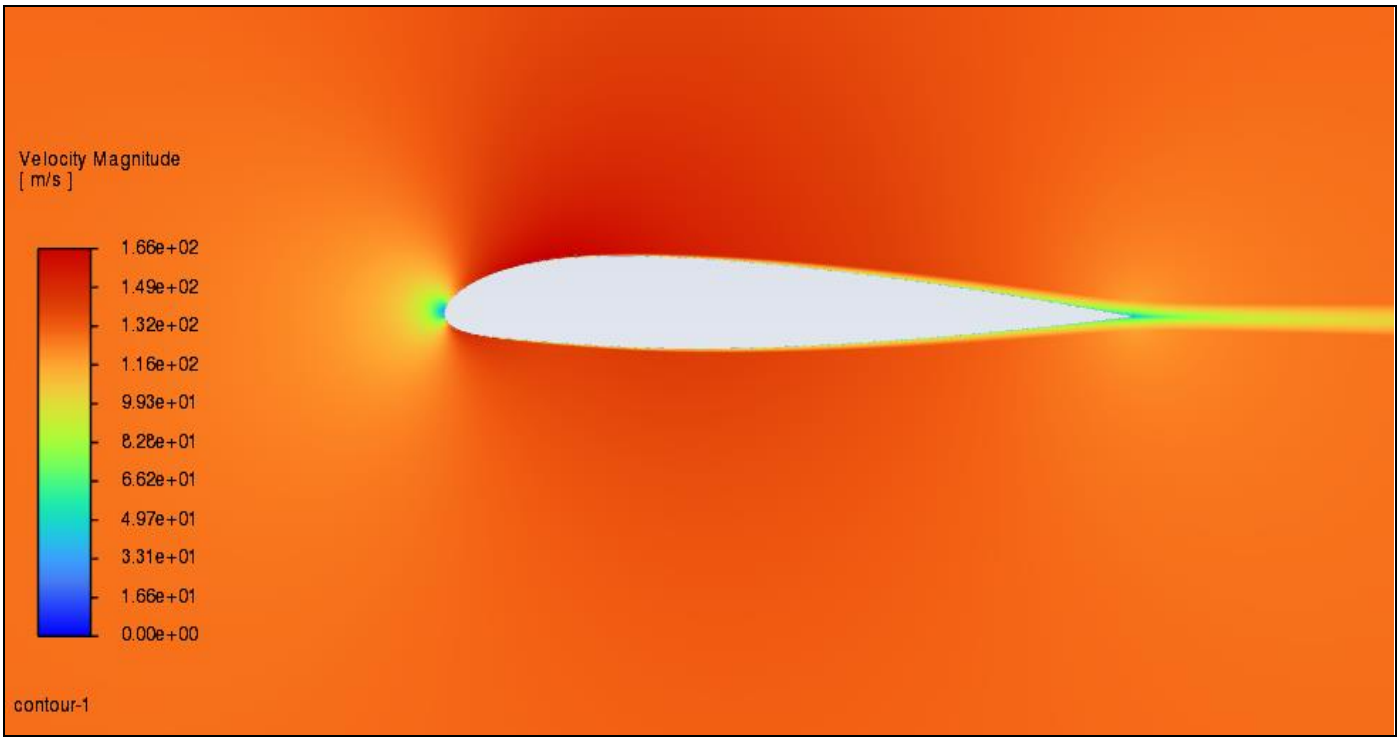

(a) 0⁰ angle of attack Re = 8.8×10⁶

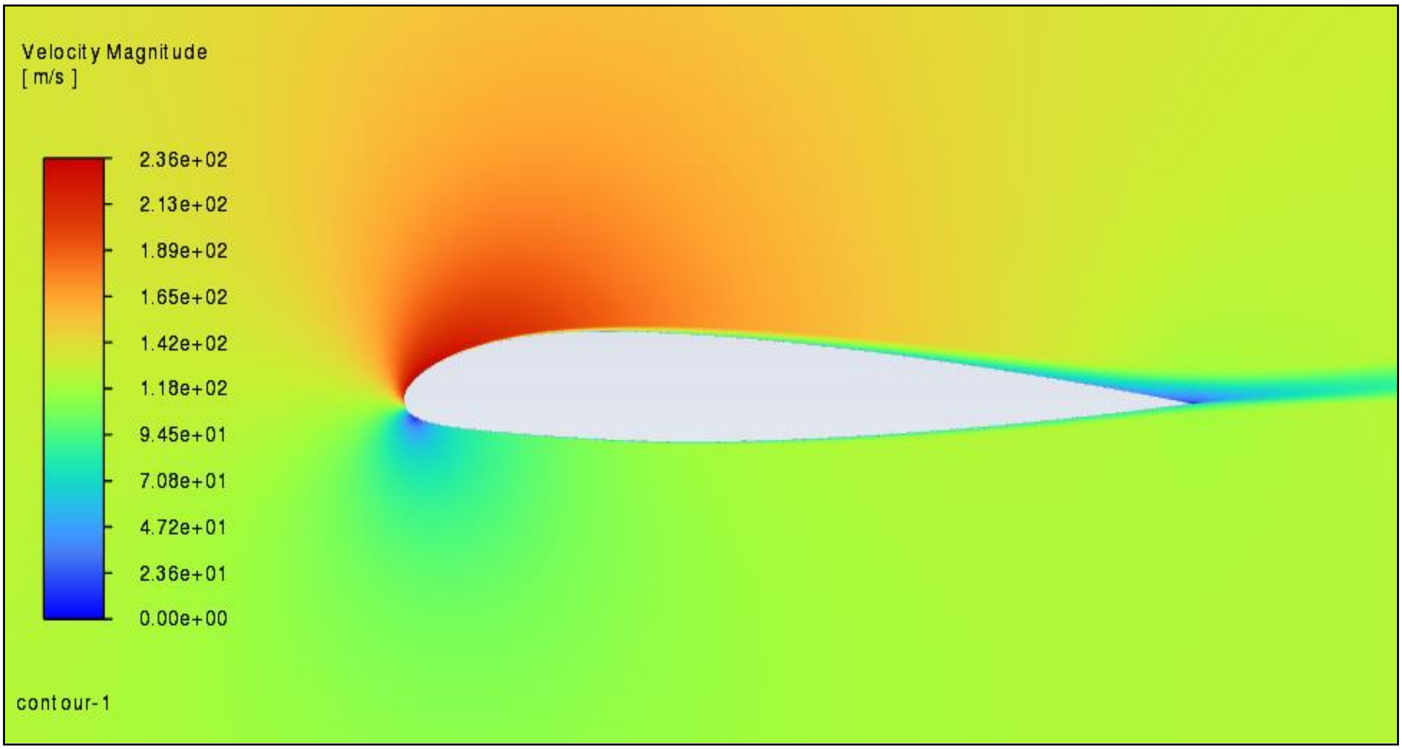

(b) 8⁰ angle of attack Re = 8.8×10⁶

International Journal of Innovative Science and Research Technology
ISSN No:-2456-2165
https://doi.org/10.38124/ijisrt/25jun567

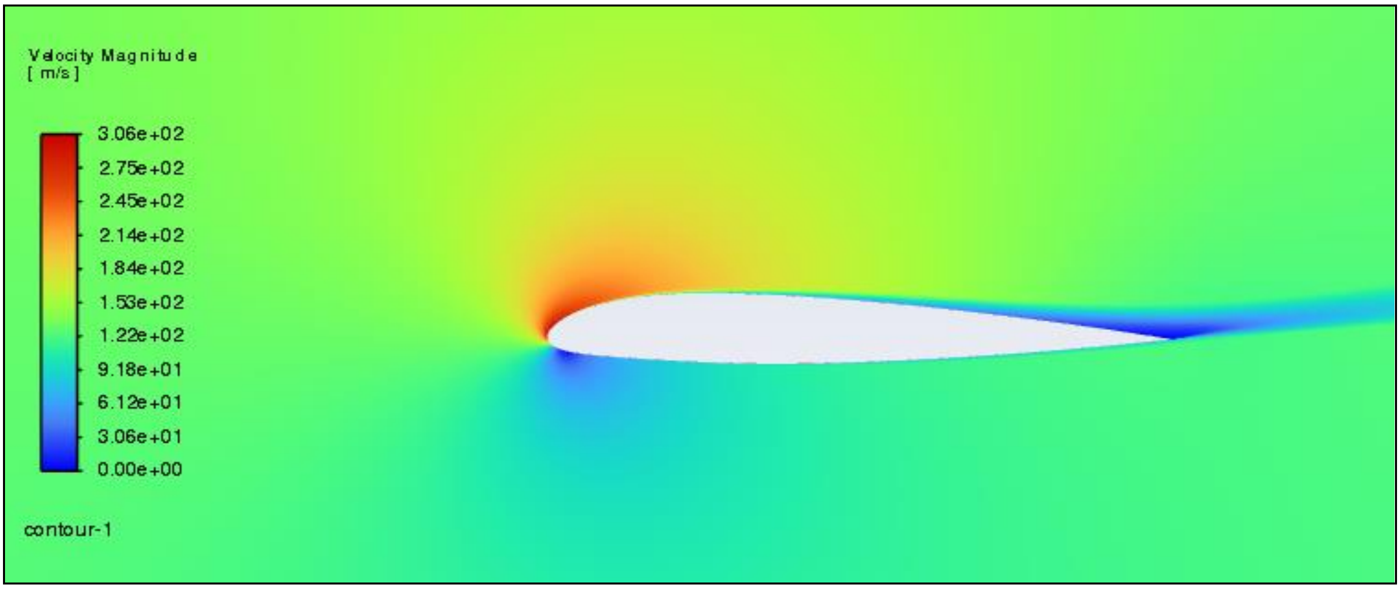

(c) 12º angle of attack Re = 8.8×10⁶

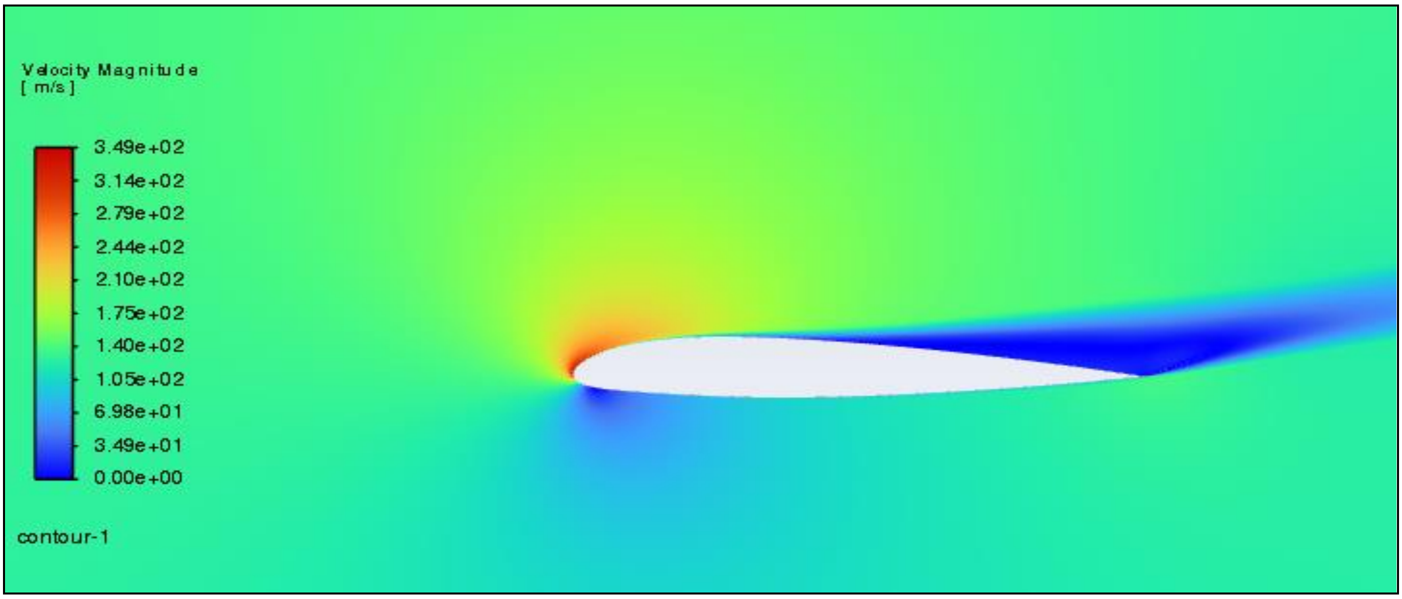

(d) 16º angle of attack Re = 8.8×10⁶

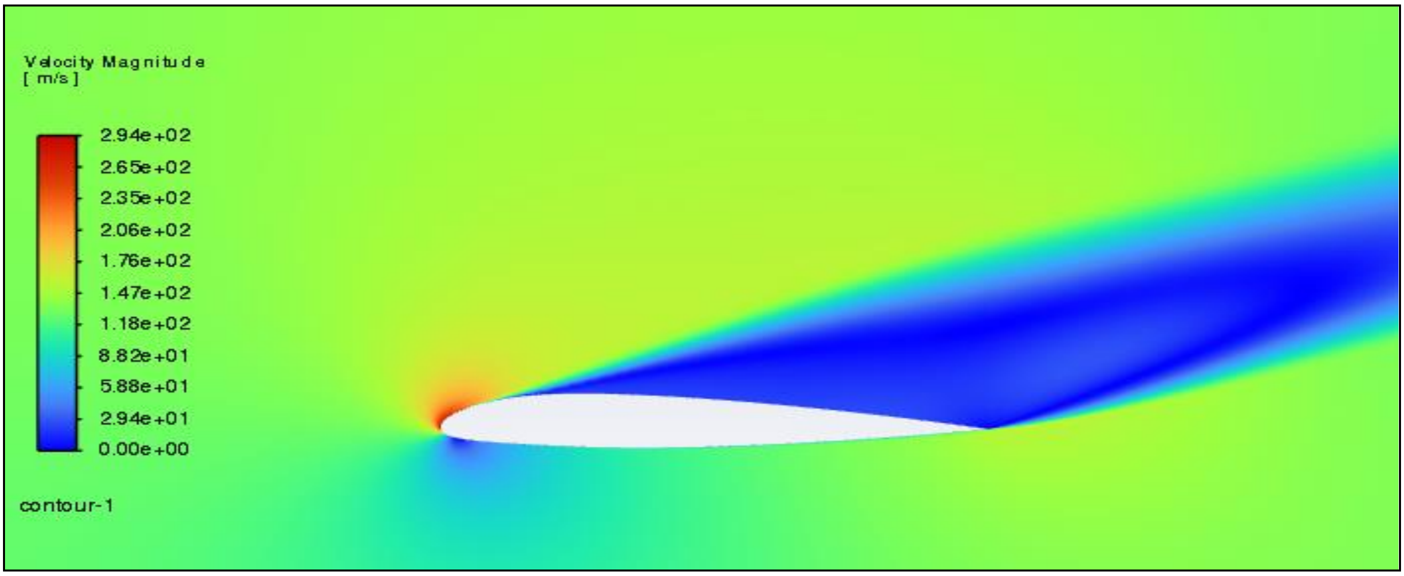

(e) 20º angle of attack Re = 8.8×10⁶

ISSN No:-2456-2165 https://doi.org/10.38124/ijisrt/25jun567

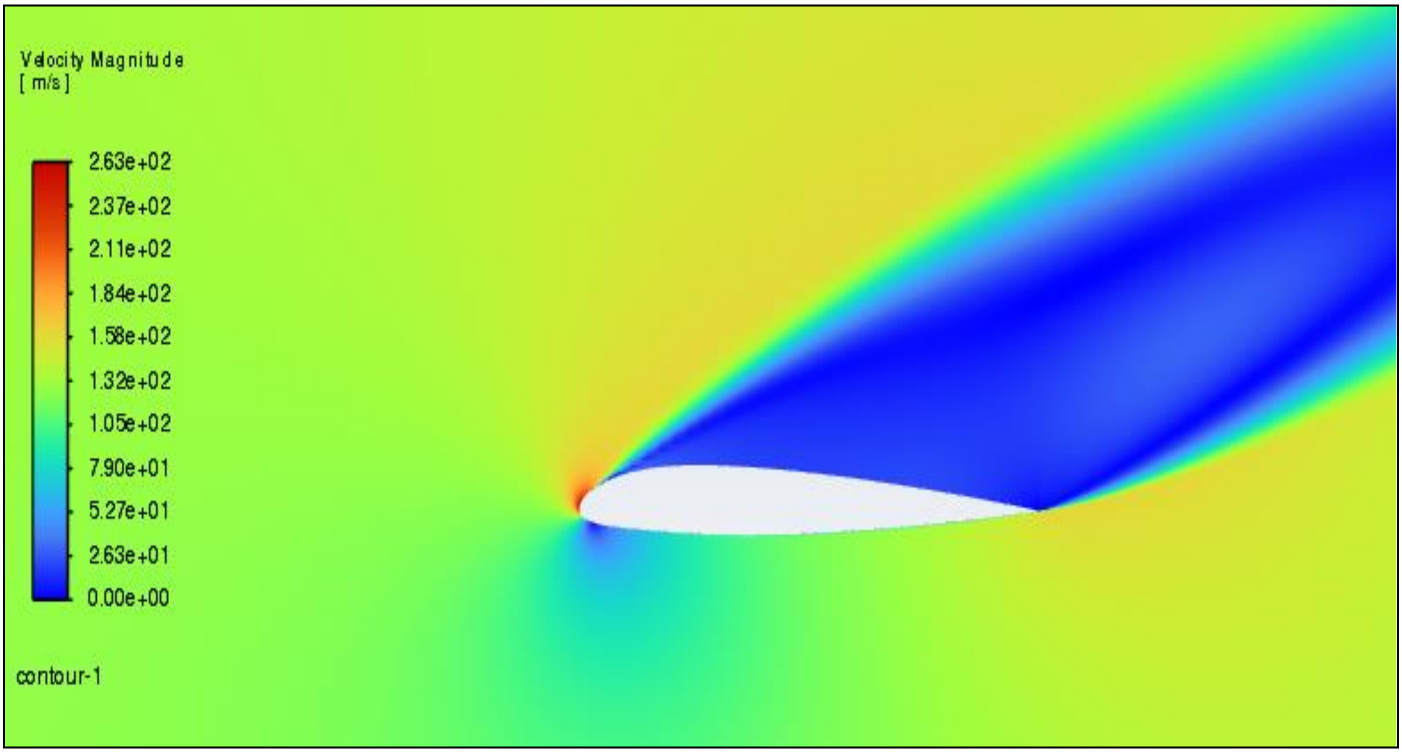

(f) 24⁰ angle of attack Re = 8.8×10^6

Fig 10 Velocity Contour for Re = 8.8×10^6

At angle 20⁰ the stall becomes more obvious. The airflow fails to reattach to the airfoil surface, and lift drops while drag increases significantly. The airfoil becomes fully stalled at angle 24⁰ a little later than that of Renolds number 6.0×10^6.

C. Effect of Angle of Attack on Airfoil Performance

Figures 11 to 16 shows that increasing the angle of attack initially increases the lift coefficient; however, beyond a specific angle, flow separation occurs, leading to a decrease in the lift coefficient with further increases in the angle of attack. Khalid (2022). Conversely, the drag coefficient increases progressively, leading to a decrease in aerodynamic efficiency beyond the stall angle. The data obtained from the simulation was validated with the data obtained from the experimental result from National Advisory Committee for Aeronautics, Report No. 824.

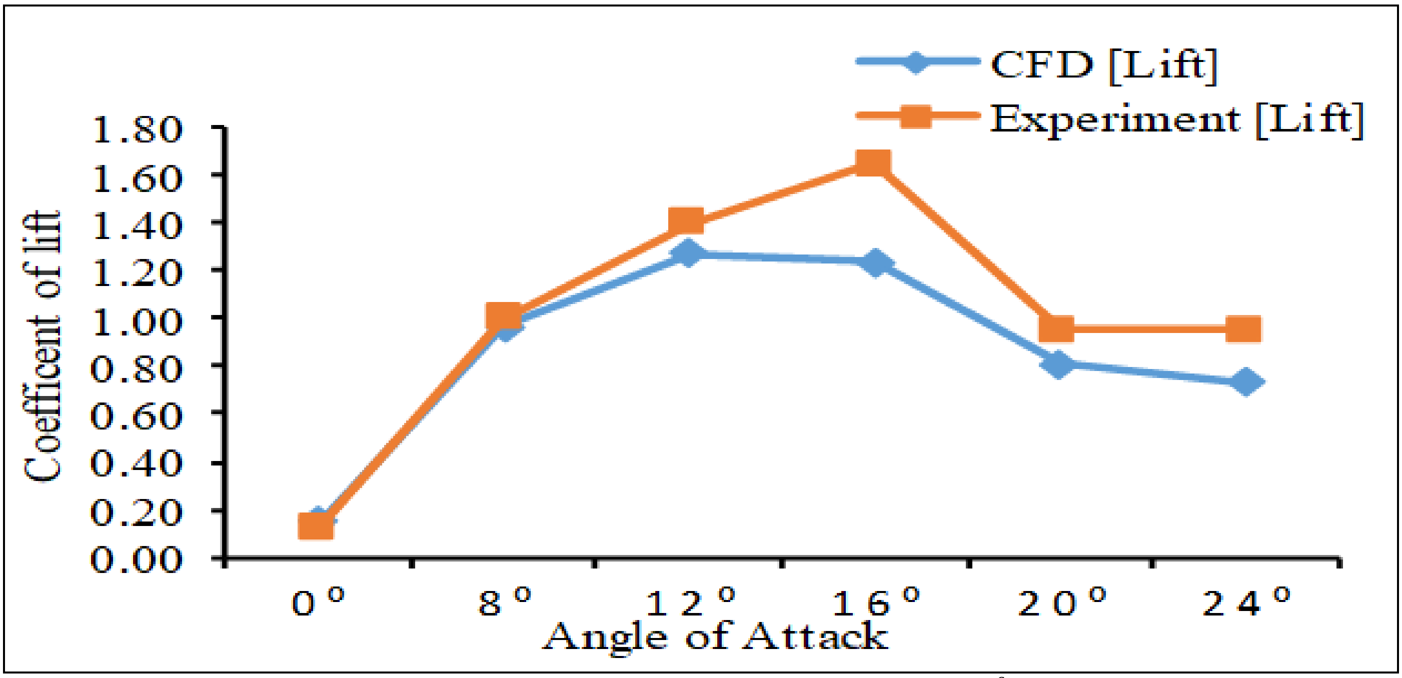

Fig 11 CFD and Experimental lift / AoA at Re = 3.0×10^6

ISSN No:-2456-2165 https://doi.org/10.38124/ijisrt/25jun567

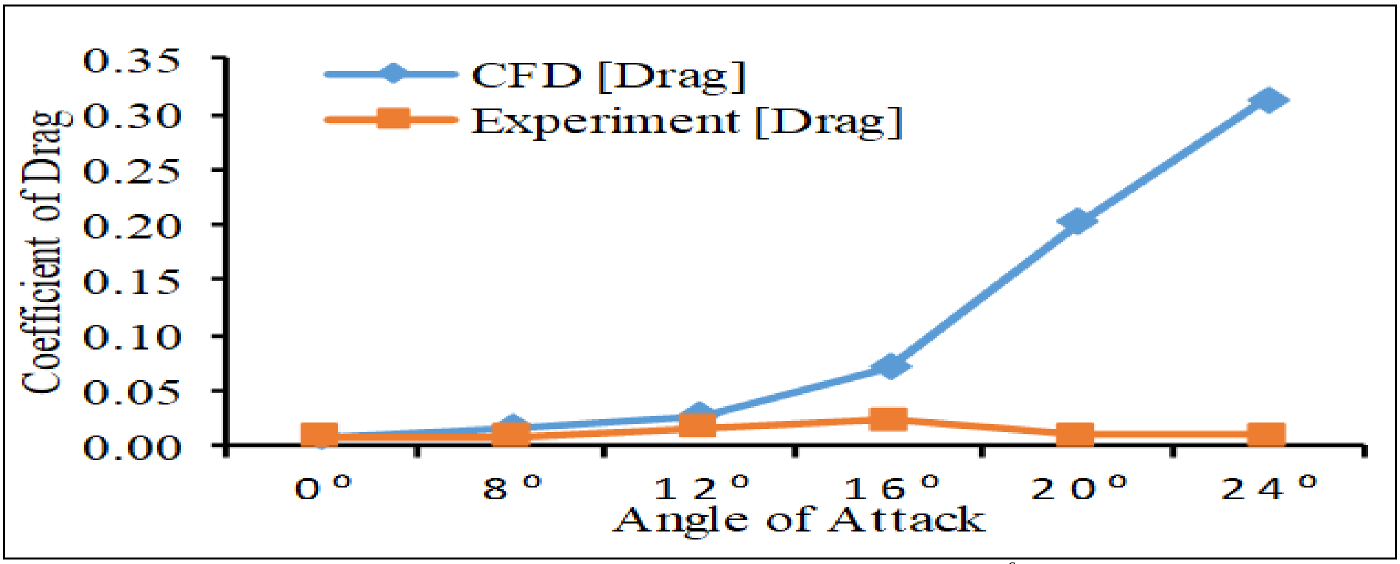

Fig 12 CFD and Experimental Drag / AoA at Re = $3.0x10^6$

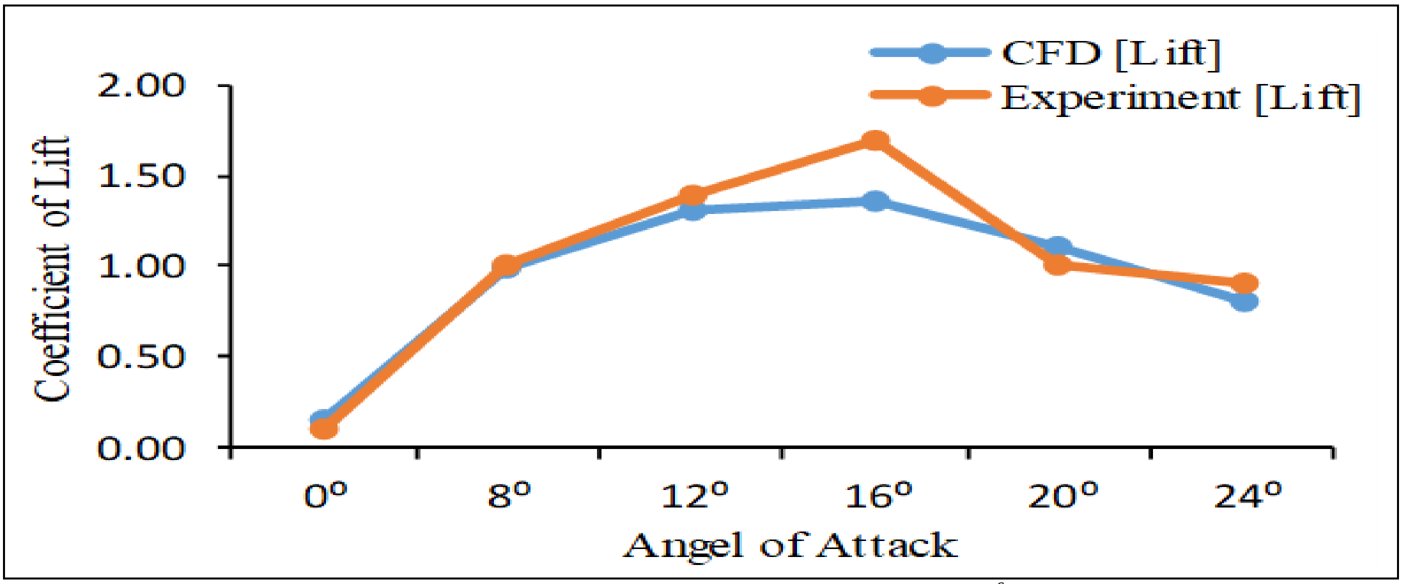

Fig 13 CFD and Experimental lift / AoA at Re = $6.0x10^6$

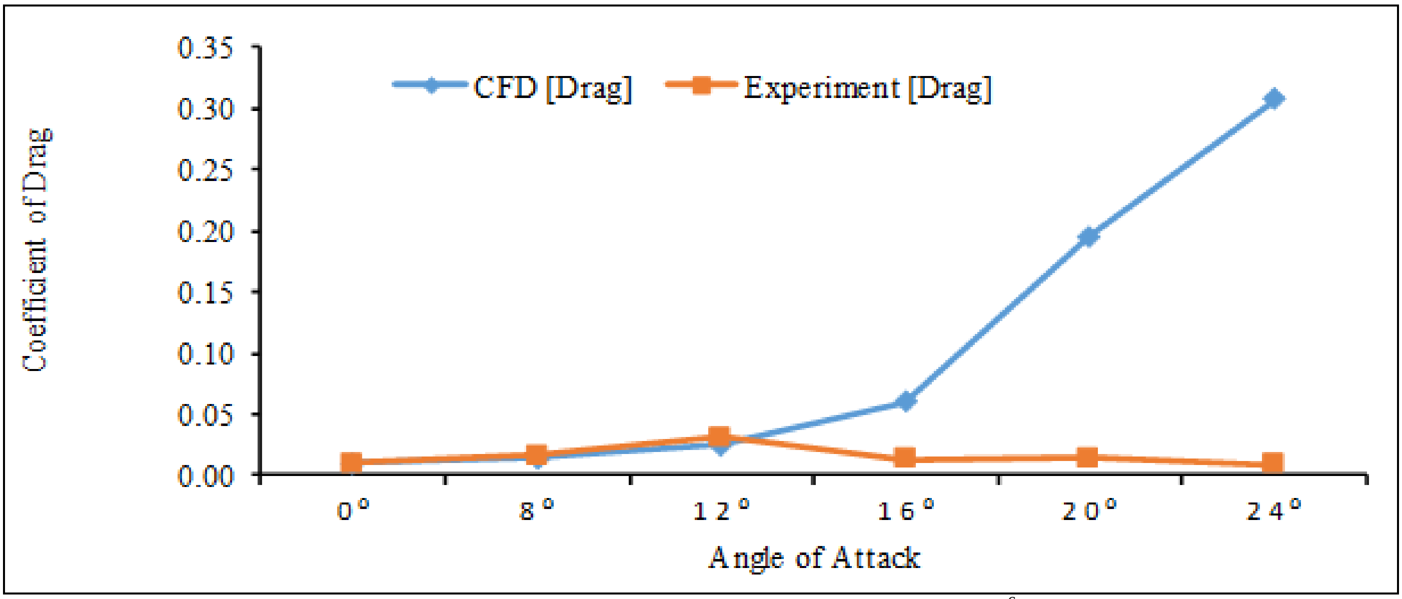

Fig 14 CFD and Experimental Drag / AoA at Re = $6.0x10^6$

ISSN No:-2456-2165 https://doi.org/10.38124/ijisrt/25jun567

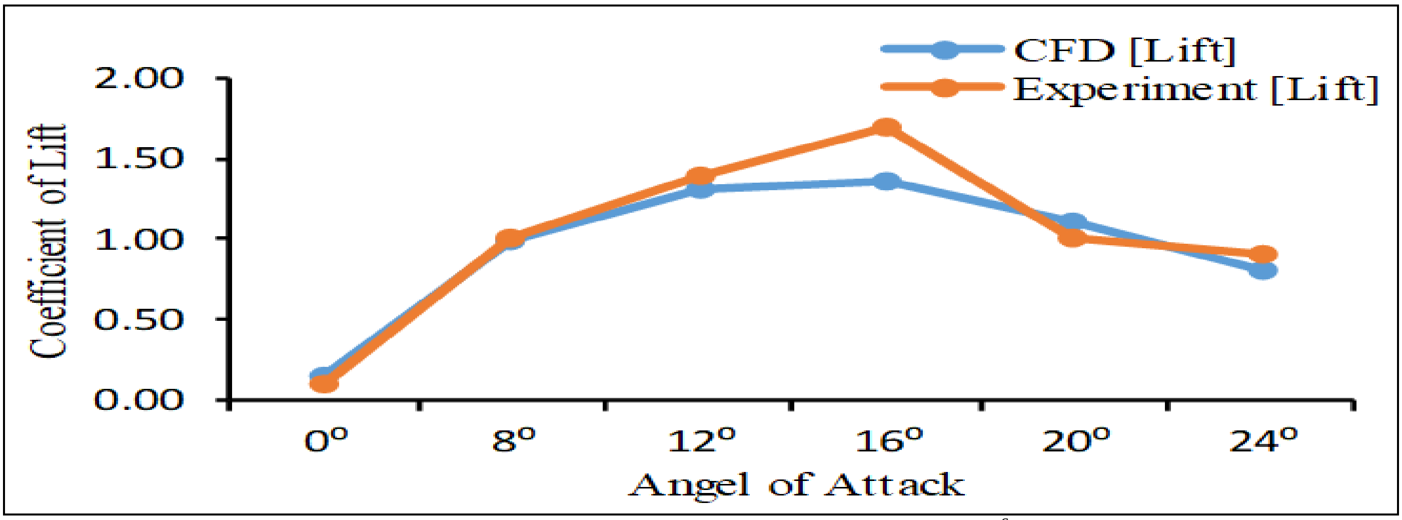

Fig 15 CFD and Experimental Lift / AoA at Re = 8.8×10^6

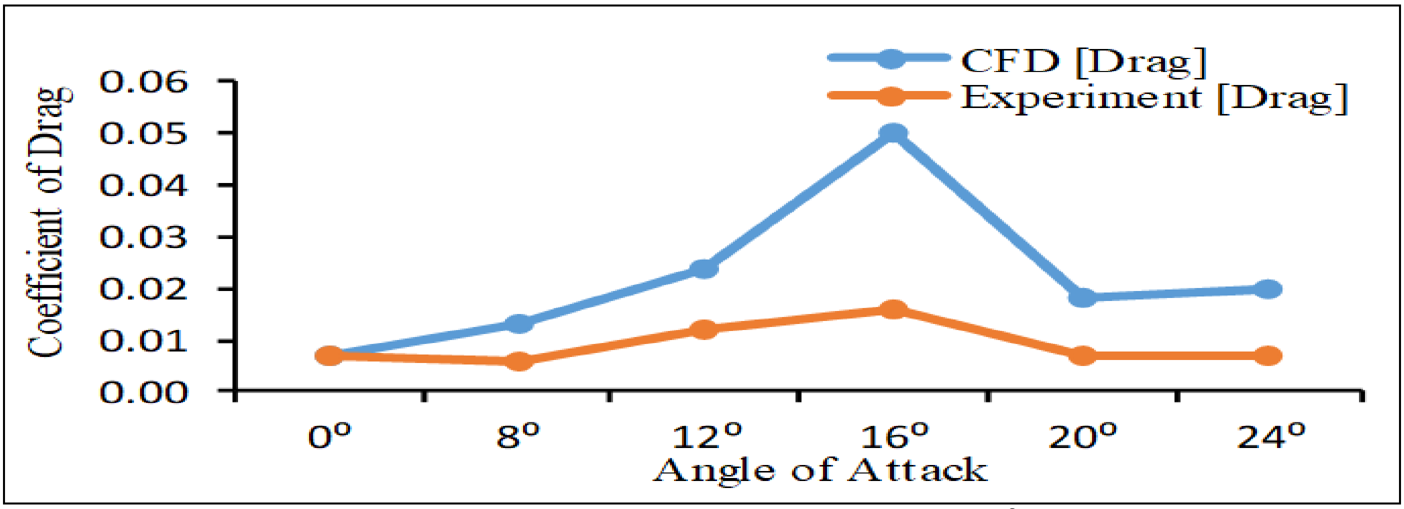

Fig 16 CFD and Experimental Drag / AoA at Re = 8.8×10^6

D. Influence of Reynolds Number on the Performance of the Airfoil

Figures 17 and 18 show the effects of change in Reynolds number. The Reynolds number (Re) significantly affects the airfoil's boundary layer behaviour, impacting lift, drag and overall efficiency of the system. It can be seen that, as Reynolds number increases, the drag coefficient decreases, which results to a higher lift-to-drag ratio. At low Reynolds numbers, the airfoil experiences higher drag and lower lift, which indicates possible laminar flow separation. Optimal performance is observed at Re = 8.8×106 with 8º where the L/D ratio reached 76.154, this suggests that higher-speed wind conditions favour better turbine efficiency.

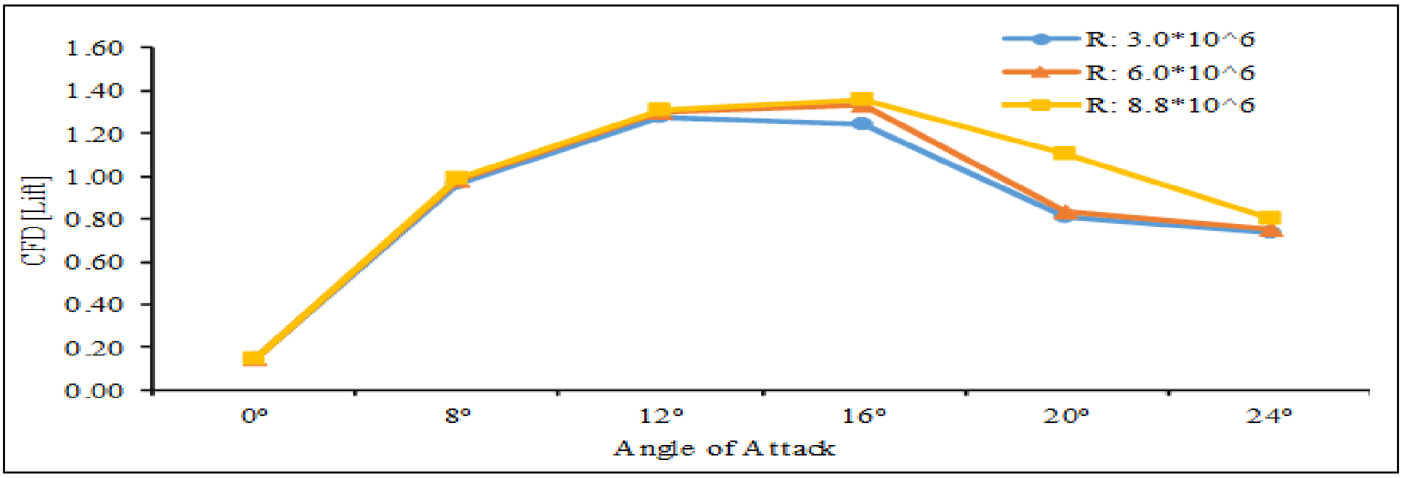

Fig 17 CFD Lift Versus AoA at Varying Reynolds Numbers

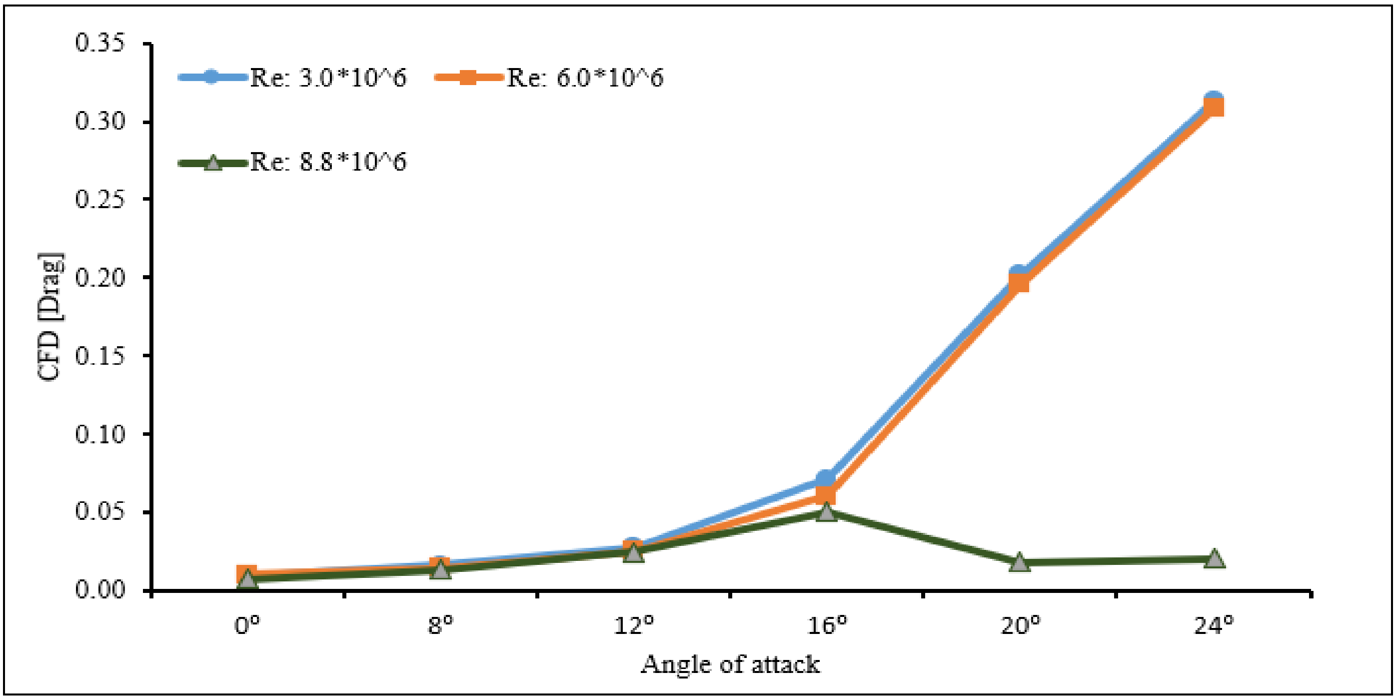

Fig 18 CFD Drag Versus AoA at Varying Reynolds Numbers

E. Result Validation

The linear regression carried out showed that the correlations (R) between the experimental-lift and CFD-lift was highly significant, especially at Re = 3.0×10^6 and Re = 8.0×10^6 with a common value of 97 and 88 for Re = 6.0×10^6 as shown in Table 3.

Table 3 Model Summary of Correlations for Result Validation

Model	R	Std. Error of the Est.	R^2 Change	F Change	df2	Sig. F Change
Lift and drag coefficients at different AoA (Re = 3.0×10⁶)						
Experimentlift/CFD lift	0.972[a]	0.108187	0.945	69.151	4	0.001
Experiment drag/CFD drag	0.181[a]	0.136484	0.033	0.136	4	0.731
Experiment Cl/Cd – CFD Cl/Cd	0.307[a]	25.344820	0.094	0.417	4	0.554
Lift and drag coefficients at different AoA (Re = 6.0×10⁶)						
Experiment lift/CFD lift	0.880[a]	0.230811	0.774	13.691	4	0.021
Experiment drag/CFD drag	0.440[a]	0.123111	0.194	0.960	4	0.383
Experiment Cl/Cd – CFD Cl/Cd	0.149[a]	30.361027	0.022	0.091	4	0.777
Lift and drag coefficients at different AoA (Re = 8.0×10⁶)						
Experiment lift/CFD lift	0.970[a]	0.121068	0.940	63.152	4	0.001
Experiment drag/CFD drag	0.914[a]	0.006753	0.836	20.430	4	0.011
Experiment Cl/Cd – CFD Cl/Cd	0.827[a]	13.179914	0.684	8.671	4	0.042

Their coefficients of determination R^2 (which justify their variations) also have very good values (94, 94 and 77 respectively). The correlation between the experimental-drag and CFD-drag also shows a significant relationship (91) at Re = 8.0×10^6 and a coefficient of determination of 83. Therefore, the linear regression performed showed that the effect of the CFD values on experimental ones was about 0.001 in many cases, thus making the model statistically significant.

To ensure that the simulation results are not influenced by mesh size, a mesh sensitivity analysis was conducted. The outcomes of this analysis at different mesh densities are summarized in Table 4. Furthermore, the dimensionless wall distance (y^+) around the airfoil was calculated and found to be less than one, indicating adequate near-wall resolution for accurate boundary layer modelling.

Table 4 Mesh Independent Test

Mesh Case	Number of Elements	y+ Value	Cl (Lift Coefficient)	Cd (Drag Coefficient)	% Change in Cl	% Change in Cd
Coarse	155,000	0.76	0.1470	0.0094	–	–
Medium	200,000	0.40	0.1461	0.0097	-0.6%	+3.09%
Fine	270,000	0.34	0.1460	0.0098	-0.07%	+1.3%

ISSN No:-2456-2165 https://doi.org/10.38124/ijisrt/25jun567

F. Discussion

The pressure plots for the three Reynolds numbers: 3.0×10^6, 6.0×10^6, and 8.8×10^6 show some similarities with increasing angle of attack, but with some important differences due to the influence of Reynolds number on flow behaviour. At an angle of attack of 0°, the pressure distribution is nearly symmetric for all three cases indicating no lift is being generated. As the angle of attack increases to 8° and 12°, a noticeable pressure difference develops between the upper and lower surfaces. The upper surface experiences a strong low-pressure region while the lower surface maintains a relatively higher pressure. This pressure difference shows the generation of lift. At 16° angle of attack, the pressure difference becomes more pronounced, especially in the case of Re = 8.8×10^6, indicating stronger lift force and delayed flow separation. While signs of stall begin to appear in the case of Reynolds number of 3.0×10^6, where the pressure gradient is less stable. At angles 20° and 24°, all three cases show evidence of stall. The low-pressure region on the upper surface expands significantly, and the pressure distribution becomes less defined, indicating separated flow. At Re = 3.0×10^6, the separation is more severe, and the pressure recovery is poor. Unlike, Re = 8.8×10^6, where the flow is a little stable even as stall has begun. For the three cases, the velocity at angle 0^o remains symmetrical as no lift is generated. As the angle of attack increases to 8° and 12°, the velocity over the upper surface increases, while it decreases slightly on the lower surface. This velocity difference indicates lift generation. As the angles of attack increases, flow separation occurs. This is visible as a region of reduced velocity on the upper surface, beginning from the mid-chord or earlier. The flow no longer follows the contour of the airfoil, indicating stall. This is common to all the Reynolds number cases. However, for Reynolds number 3.0×10^6 at 16^o, a large, separated flow region is already visible. The flow behaviour around the airfoil shows a symmetric flow at low angles of attack and flow separation at higher angles of attack [11], at low angles of attack, the flow over a well-designed airfoil remains attached, creating a strong pressure difference between the upper and lower surfaces, and leading to efficient lift production. As the angle of attack increases beyond a critical point, the adverse pressure gradient over the upper surface grows stronger, eventually causing the boundary layer to separate, which leads to stall. Also, the differences in flow behaviour at varying Reynolds numbers agree with the work of [25], that at higher Reynolds numbers, airfoils exhibit delayed flow separation because the boundary layer tends to have higher momentum, making it better able to resist adverse pressure gradients. This explains why at Re = 8.8×10^6, the flow remains coherent even up to 16° and 20°, compared to the lower Reynolds number cases where separation starts earlier. As reported by [26], the rapid pressure recovery and thick separation bubbles indicate the beginning of early stall at low Reynolds numbers. This can be seen in the contours at Re = 3.0×10^6, where the pressure field becomes disorganized earlier. The gradual expansion of the low-velocity region along the airfoil surface with increasing angle of attack supports the aerodynamic model of stall development, where flow separation begins near the trailing edge and gradually moves forward as angle of attack increases, similar to the work of [10]. The optimal performance for the NACA 23012 airfoil was found at 8° angle of attack and Reynolds number 8.8×10^6. The airfoil exhibits a high lift coefficient with a relatively low drag, resulting in a favourable lift-to-drag ratio. These findings seem promising for the design of Darrieus wind turbines known for their lift-based approach. As a result, aerodynamic efficiency is enhanced which in turn directly increases torque generation, power output, and the overall performance maximization.

IV. CONCLUSION

The CFD simulation of the NACA 23012 airfoil under varying angles of attack and Reynolds numbers has provided valuable insights into its aerodynamic performance. The results show that as the angle of attack increases, lift improves up to a certain point typically between 12° and 16° after which flow separation and stall occur, leading to a reduction in aerodynamic efficiency. Higher Reynolds numbers enhance the airfoil's performance by delaying boundary layer separation, promoting smoother airflow, and increasing lift. The pressure and velocity contour plots clearly illustrate these features, revealing how flow behaviour transitions from attached to separated conditions at higher angles. Overall, the optimal performance of the NACA 23012 airfoil is achieved at moderate angles of attack and high Reynolds numbers, making it well-suited for applications like vertical axis wind turbines, especially in low to moderate wind speed environments. The results from this research help in predicting when lift is strong and when stall occurs for NACA 23012 airfoil. The findings also guide the use of pitch control systems to prevent stall and optimize power output, strongly improving the efficiency, durability, and safety of wind turbines. These findings can be used to assist in further optimization and structural design improvements for energy harvesting turbine blades.

REFERENCES

[1]. Yoro, K. O., & Daramola, M. O. (2020). CO2 emission sources, greenhouse gases, and the global warming effect. In Advances in carbon capture (pp. 3-28). Woodhead Publishing.

[2]. Siddik, M., Islam, M., Zaman, A. K. M. M., & Hasan, M. (2021). Current status and correlation of fossil fuels consumption and greenhouse gas emissions. Int. J. Energy Environ. Econ, 28, 103-119.

[3]. Dahlan, N. Y., Ahmad, N., Ilham, N. I., & Yusoff, S. H. (2022). Energy security: role of renewable and low-carbon technologies. In Handbook of energy and environmental security (pp. 39-60). Academic Press.

[4]. Izanloo, M., Noorollahi, Y., & Aslani, A. (2021). Future energy planning to maximize renewable energy share for the south Caspian Sea climate. Renewable Energy, 175, 660-675.

[5]. Eltayeb, W. A., Somlal, J., Kumar, S., & Rao, S. K. (2023). Design and analysis of a solar-wind hybrid renewable energy tree. Results in Engineering, 17, 100958.

[6]. Mostafaeipour, A., Rezaei, M., Jahangiri, M., & Qolipour, M. (2020). Feasibility analysis of a new tree-shaped wind turbine for urban application: A case study. Energy & Environment, 31(7), 1230-1256.
[7]. Jha, A. R. (2010). Wind turbine technology. Boca Raton, Florida, USA: CRC Press.
[8]. Miliket, T. A., Ageze, M. B., & Tigabu, M. T. (2022). Aerodynamic performance enhancement and computational methods for H-Darrieus vertical axis wind turbines. International Journal of Green Energy, 19(13), 1428-1465.
[9]. Silva, M. F., Malheiro, B., Guedes, P., & Ferreira, P. (2020). Airfoil selection and wingsail design for an autonomous sailboat. In Robot 2019: Fourth Iberian Robotics Conference: Advances in Robotics, Volume 1 (pp. 305-316). Springer International Publishing.
[10]. Anderson, J. D. (2010). Fundamentals of Aerodynamics (5th ed.). McGraw-Hill Education.
[11]. Abbott, I. H., & Von Doenhoff, A. E. (1959). Theory of Wing Sections: Including a Summary of Airfoil Data. Dover Publications.
[12]. Karamcheti, K. (1980). Principles of Ideal-Fluid Aerodynamics. Krieger Publishing Company.
[13]. Seifi Davari, H., Seify Davari, M., Botez, R., & Chowdhury, H. (2023). Maximizing the peak lift-to-drag coefficient ratio of airfoils by optimizing the ratio of thickness to the camber of airfoils. Sustainable Earth Trends, 3(4), 46-61.
[14]. Rizwan, M., Yousuf, F., & Khan, M. S. (2017). CFD Analysis of NACA 0012 for Wind Turbine Blades. International Journal of Mechanical and Production Engineering, 5(5), 100–104.
[15]. Ahmed, N., & Ismail, M. (2014). CFD Simulation for Airfoil NACA 4412. International Journal of Engineering Trends and Technology, 15(2), 61–66.
[16]. Subhodh S Ghadge1 , Nandakishor H Murhekar2 , Amol L Khatode (2021). CFD Analysis carried out on Wind Turbine Blade for Different Angles of Attack and Various Reynolds Number. © 2021 IJCRT | Volume 9, Issue 1 January 2021 | ISSN: 2320-2882.
[17]. Khalid, M. H. (2022). CFD Analysis of NACA 0012 Aerofoil to Investigate the Effect of Increasing Angle of Attack on Coefficient of Lift and Coefficient of Drag. Journal of Studies in Science and Engineering, 2(1), 74–86. https://doi.org/10.53898/josse2022216.
[18]. Tullis, S., et al. (2011). "Modelling and testing of modified helical vertical-axis wind turbines." Wind Engineering, 35(3), 361–376.
[19]. Rezaeiha, A., Montazeri, H., & Blocken, B. (2017). "Towards optimal aerodynamic design of vertical axis wind turbines: Impact of solidity and number of blades." Energy Conversion and Management, 153, 362–377.
[20]. Airfoil Tool database (2025). http://airfoiltools.com/airfoil/details?airfoil=naca23012-il Accessed April 25, 2025.
[21]. Julius, M. O., Adio, S., Soji-Adekunle, A., Ishaq, A., Akigbade, T., & Fatai, B. (2025). Unsteady aerodynamic performance of spiked and unspiked aloe vera-inspired aerofoils at low reynolds number. LAUTECH Journal of Engineering and Technology, 19(1), 54-64.
[22]. Semprini Cesari, G. (2023). Active flow control of the turbulent boundary layer over a NACA4412 wing profile for skin friction drag reduction.
[23]. Jo, B. W., & Majid, T. (2022). Aerodynamic analysis of camber morphing airfoils in transition via computational fluid dynamics. Biomimetics, 7(2), 52.
[24]. Versteeg H. K. and W. Malalasekera (2007). Computational Fluid Dynamics: The Finite Volume Method. 2nd Eddition. Pearson Education Limited. ISBN 9780131274983.
[25]. McCroskey, W. J. (1987). The Phenomenon of Stall. NASA Technical Memorandum 86890.
[26]. Schlichting, H., & Gersten, K. (2016). Boundary-Layer Theory (9th ed.). Springer
[27]. Menter, F. R. (1994). Two-equation eddy-viscosity turbulence models for engineering applications. AIAA Journal, 32(8), 1598–1605. https://doi.org/10.2514/3.12149.